

GSR: Graph Smooth Null-Space Representation for Inverse Problems

Romario Gualdrón-Hurtado*, Roman Jacome*, Rafael S. Suarez, Henry Arguello
 Universidad Industrial de Santander, Colombia, 680002

{yesid2238324, rajaccar, rafael2269082}@correo.uis.edu.co, henarfu@uis.edu.co

Abstract

Inverse problems in imaging are ill-posed, leading to infinitely many solutions consistent with the measurements due to the non-trivial null-space of the sensing matrix. Common image priors promote solutions on the general image manifold, such as sparsity, smoothness, or score function. However, as these priors do not constrain the null-space component, they can bias the reconstruction. Thus, we aim to incorporate meaningful null-space information in the reconstruction framework. Inspired by smooth image representation on graphs, we propose Graph-Smooth Null-Space Representation (GSR), a mechanism that imposes structure only into the invisible component. Particularly, given a graph Laplacian, we construct a null-restricted Laplacian that encodes similarity between neighboring pixels in the null-space signal, and we design a low-dimensional projection matrix from the p -smoothest spectral graph modes (lowest graph frequencies). This approach has strong theoretical and practical implications: i) improved convergence via a null-only graph regularizer, ii) better coverage, how much null-space variance is captured by p modes, and iii) high predictability, how well these modes can be inferred from the measurements. GSR is incorporated into well-known inverse problem solvers, e.g., PnP, DIP, and diffusion solvers, in four scenarios: image deblurring, compressed sensing, demosaicing, and image super-resolution, providing consistent improvement of up to 4.3 dB over baseline formulations and up to 1 dB compared with end-to-end learned models in terms of PSNR.

1. Introduction

Recovering an image from a limited number of noisy measurements requires estimating a solution to an undetermined inverse problem, which is of the form

$$\mathbf{y} = \mathbf{H}\mathbf{x}^* + \boldsymbol{\omega}, \quad \boldsymbol{\omega} \sim \mathcal{N}(\mathbf{0}, \sigma^2 \mathbf{I}). \quad (1)$$

where $\mathbf{y} \in \mathbb{R}^m$ denotes the measurement vector, $\mathbf{x}^* \in \mathbb{R}^n$ is the unknown target image, $\mathbf{H} \in \mathbb{R}^{m \times n}$ is the sensing matrix with $m \leq n$, and $\boldsymbol{\omega}$ models additive Gaussian noise. This formulation is used in a broad range of imaging tasks

by using a proper structure of \mathbf{H} . Compressed sensing (CS) tasks employ dense sensing matrices [5]. Image restoration problems, such as deblurring [53], inpainting [51], and super-resolution [46], are modeled by structured Toeplitz or block-diagonal matrices. In medical imaging, modalities like magnetic resonance imaging (MRI) [26] and computed tomography (CT) [2] use structured physics-based operators (e.g., undersampled Fourier or Radon transforms). The formulation in (1) becomes ill-posed due to matrix instability and/or the undersampling scheme. Therefore, incorporating prior knowledge or regularization is essential to promote reconstructions that are consistent with the expected structure of \mathbf{x}^* [4]. The estimation of \mathbf{x}^* is commonly formulated as a variational problem that combines a data-fidelity term and a regularization term:

$$\hat{\mathbf{x}} = \arg \min_{\tilde{\mathbf{x}}} \underbrace{\frac{1}{2} \|\mathbf{H}\tilde{\mathbf{x}} - \mathbf{y}\|_2^2}_{\text{data fidelity: } g(\tilde{\mathbf{x}})} + \lambda \underbrace{f(\tilde{\mathbf{x}})}_{\text{prior}} \quad (2)$$

where $g(\tilde{\mathbf{x}})$ enforces consistency with the measurements and $f(\tilde{\mathbf{x}})$ incorporates prior knowledge about the structure of \mathbf{x}^* . Recent advances have introduced data-driven regularizers for $f(\tilde{\mathbf{x}})$, most notably Plug-and-Play (PnP) [6, 20, 48, 52] and Regularization by Denoising (RED) [9, 34, 35], which have achieved remarkable success across a wide range of imaging tasks [20] by implicitly promoting solutions within the training image dataset manifold i.e., well-trained denoiser learns the data score-function [27]. PnP and RED use learned denoisers, allowing the integration of powerful deep restoration networks within algorithms [27, 44]. Despite their versatility and success, these priors operate in the image domain and do not explicitly exploit the structure of \mathbf{H} , including its null-space (NS). Only a portion of \mathbf{x}^* is observable through \mathbf{H} . The range-null-space decomposition (RNSD) states that any $\mathbf{x} \in \mathbb{R}^n$ vector is decomposed as $\mathbf{x} = \mathbf{x}_r + \mathbf{x}_n$, where $\mathbf{x}_r = \mathbf{P}_r \mathbf{x}$ denotes the component lying in the range space of \mathbf{H} , with $\mathbf{P}_r = \mathbf{H}^\dagger \mathbf{H}$, and $\mathbf{x}_n = \mathbf{P}_n \mathbf{x}$ denotes the component lying in its NS, with the NS projector $\mathbf{P}_n = \mathbf{I} - \mathbf{H}^\dagger \mathbf{H}$. \mathbf{x}_n is invisible to \mathbf{H} because it belongs its NS, defined as

$$\begin{aligned} \text{Null}(\mathbf{H}) &= \{\mathbf{x} \in \mathbb{R}^n : \mathbf{H}\mathbf{x} = \mathbf{0}\} \\ &= \{\mathbf{x} : \mathbf{x} \perp \mathbf{h}_j, \forall j \in \{1, \dots, m\}\}, \end{aligned}$$

*Equal contribution.

where $\mathbf{h}_j \in \mathbb{R}^n$ is the j -th row of \mathbf{H} . This interpretation has inspired approaches that explicitly exploit $\text{Null}(\mathbf{H})$. Null-Space Networks (NSN) [41] and Deep Decomposition [7] operate across the entire $\text{Null}(\mathbf{H})$, treating all invisible directions as equally relevant, neglecting the fact that natural, perceptually plausible images occupy only a low-dimensional manifold within that space [17]. To address this gap, the recent Nonlinear Projections of the Null-Space (NPN) framework [17] introduces a learnable low-dimensional NS projection matrix $\mathbf{S} \in \mathbb{R}^{p \times n}$, with $p \leq (n - m)$. \mathbf{S} is designed depending on the inverse problem, making its rows orthogonal to \mathbf{H} , then \mathbf{S} is optimized jointly a NS component predictor $G(\mathbf{y}) \equiv \mathbf{S}\mathbf{x}^*$ to adapt the $\text{span}(\mathbf{S})$ into a subspace of $\text{Null}(\mathbf{H})$. During reconstruction, NPN penalizes deviations $\|G(\mathbf{y}) - \mathbf{S}\tilde{\mathbf{x}}\|_2^2$. However, natural images occupy a low-dimensional, structured subset inside $\text{Null}(\mathbf{H})$, so blindly learning an arbitrary $\text{span}(\mathbf{S}^\top) \subset \text{Null}(\mathbf{H})$ can waste capacity and induce bias. In this work, we present a principled framework that provides a new representation of the NS, enabling the optimal selection of informative NS directions. To address this issue, we took into account two main optimality criteria:

Coverage: *How much of the null-space of \mathbf{H} is represented with the projection matrix \mathbf{S} .*

Predictability: *How easily can the projections $\mathbf{S}\mathbf{x}$ be estimated from the measurements \mathbf{y} only.*

Inspired by the graph (smooth) representation of images [28, 29], we introduce Graph-Smooth Null-Space Representation (GSNR) to overcome the shortcomings of NS representation and prediction. Different from the well-studied graph-structure preserving approach in imaging inverse problems [19, 28] that promotes smoothness over the image \mathbf{x} , our approach is the first to endow the NS component \mathbf{x}_n with a graph structure, defined through a sparse, positive semidefinite graph Laplacian $\mathbf{L} \succeq \mathbf{0}$, such as 4/8-nearest-neighbor (NN) image grid whose edge weights encode local pixel similarity. We form the *null-restricted Laplacian* $\mathbf{T} := \mathbf{P}_n \mathbf{L} \mathbf{P}_n$ on $\text{Null}(\mathbf{H})$. Via spectral graph theory, we construct the graph-smooth NS projection matrix \mathbf{S} as the p -smoothest NS modes, which corresponds to the p first graph Fourier modes. The proposed GSNR changes how we solve inverse problems by providing exact structure information where the sensor is blind. By selecting the p -smoothest eigenmodes of the null-restricted Laplacian, our method (i) reduces hallucinations and bias by constraining only the invisible component, not the whole image; (ii) improves conditioning, leading to faster and more stable convergence across PnP, DIP, and diffusion solvers; (iii) increases data efficiency by capturing most null-space variation with small p (high coverage) and by targeting the modes that are easiest to infer from measurements (high predictability); and (iv) offers operational di-

agnostics coverage/predictability curves that allows selecting p and justify regularization objectively. Because it is plug-compatible with standard pipelines and agnostic to the forward operator, the approach scales across different imaging tasks, turning an ill-posed ambiguity into a structured, measurable, and learnable component. The proposed construction has the following benefits:

1. Selected graph-smooth null-space components produce high coverage at low dimensionality projection, i.e., small p (Theorem 1 and Theorem 2).
2. Predicting the p null-space components from \mathbf{y} using a GSNR is easier than the ones obtained with a common null-space basis (Proposition 1).
3. Predicted graph null-space components can be incorporated via regularization into solvers such as PnP, Deep Image Prior, and Diffusion Models.

2. Related Work

Variational and learned priors. A common scheme to solve (2) is proximal gradient descent (PGD) [30]. Recently, PnP [20] and RED [35] methods have replaced the proximal operator of $f(\tilde{\mathbf{x}})$ with learned denoisers, enabling the incorporation of data-driven priors without requiring an explicit analytic form [17]. Although these frameworks achieve state-of-the-art performance, they leave $\text{Null}(\mathbf{H})$ largely unconstrained; denoisers may freely modify components that are invisible to the sensing operator.

Nonlinear Projections of the Null-Space (NPN). To explicitly regularize image unobserved components, [17] introduced a task-specific low-dimensional projection within $\text{Null}(\mathbf{H})$, enforcing consistency between learned NS predictions and reconstructions. Building on this principle, we propose GSNR, which incorporates graph-smoothness analysis to guide the selection of a structured null-subspace. Our design ensures that the learned projection aligns with the intrinsic geometry of the data, yielding NS components that are both predictable from the measurements and consistent with the graph-induced smoothness prior.

Graph theory in imaging inverse problems. Variational regularization methods address inverse problems by imposing smoothness or sparsity priors that constrain the solution space. Total variation [38] enforces pixel-wise smoothness, whereas wavelet-based sparsity priors [13] promote sparse representations of images in the transform domain via soft-thresholding. Although these priors improve stability, they are typically limited to local structures and often oversmooth fine textures or complex geometries. To better capture local dependencies, graph-based and non-local regularization methods have been reintroduced. [32] proposed an adaptive nonlocal regularization framework that jointly estimates the image and the graph that encodes patch similarities. However, like classical priors, this framework operates solely on the reconstruction and doesn't constrain the image component lying in $\text{Null}(\mathbf{H})$.

3. Graph-Smooth Null-Space Representation

3.1. Preliminaries: Graphs

Graphs provide a geometric representation of data, where vertices correspond to data elements (e.g., pixels or image patches) and weighted edges encode pairwise similarities between them [42]. Signals defined on weighted undirected graphs are mathematically denoted by $\mathcal{G} = (\mathcal{V}, \mathcal{E}, \mathbf{W})$, where \mathcal{V} is the vertex set with $|\mathcal{V}| = n$, $\mathcal{E} \subseteq \mathcal{V} \times \mathcal{V}$ is the edge set, and $\mathbf{W} \in \mathbb{R}^{n \times n}$ is the symmetric weighted adjacency matrix with $\mathbf{W}_{ij} > 0$ if $(i, j) \in \mathcal{E}$ and $\mathbf{W}_{ij} = 0$ otherwise. The unnormalized graph Laplacian is

$$\mathbf{L} = \mathbf{D} - \mathbf{W}, \quad (\mathbf{L}\mathbf{x})_i = \sum_j \mathbf{W}_{ij}(\mathbf{x}_i - \mathbf{x}_j), \quad (3)$$

where the diagonal degree matrix $\mathbf{D} = \text{diag}(d_1, \dots, d_n)$ accomplishes $d_i = \sum_j \mathbf{W}_{ij}$. Its Dirichlet energy is

$$\mathbf{x}^\top \mathbf{L}\mathbf{x} = \frac{1}{2} \sum_{i,j} \mathbf{W}_{ij}(\mathbf{x}_i - \mathbf{x}_j)^2, \quad (4)$$

which penalizes discrepancies across edges with large weights. For symmetric \mathbf{W} , \mathbf{L} is real symmetric positive semidefinite (SPSD) with eigenpairs $\{(\lambda_\ell, \mathbf{v}_\ell)\}_{\ell=0}^{n-1}$, $0 = \lambda_0 \leq \lambda_1 \leq \dots$, $\mathbf{v}_0 \propto \mathbf{1}$ on connected graphs. Eigenvectors with small λ_ℓ vary slowly across high-weight edges, motivating the interpretation of λ as a graph frequency. For the usage of \mathbf{L} , we focus on two graph topologies [29]:

1. **4NN**: This promotes piecewise smoothness aligned with the coordinate axes and attenuates horizontal/vertical fluctuations, yielding an anisotropic (axis-biased) smoothing effect. Here, $\mathcal{E}_4 = \{(i, j) : \|\mathbf{p}_i - \mathbf{p}_j\|_1 = 1\}$, $\mathbf{W}_{ij} = \mathbf{1}_{(i,j) \in \mathcal{E}_4}$, with $\mathbf{p}_i \in \mathbb{Z}^2$ pixel coordinates.
2. **8NN**: This reduces orientation bias and more closely approximates an isotropic Laplace operator, promoting rotation-invariant piecewise smoothness and suppressing fluctuations uniformly across directions. Here, $\mathcal{E}_8 = \{(i, j) : \|\mathbf{p}_i - \mathbf{p}_j\|_\infty = 1\}$, $\mathbf{W}_{ij} = w_o \mathbf{1}_{\|\cdot\|_2=1} + w_d \mathbf{1}_{\|\cdot\|_2=\sqrt{2}}$, where $w_d = w_o/\sqrt{2}$.

Nevertheless, we extend the analysis of the proposed approach to other topologies in Supp. A4.1.

3.2. Graph-smooth null modes

We study smoothness within the NS by restricting the Laplacian to

$$\mathbf{T} = \mathbf{P}_n \mathbf{L} \mathbf{P}_n, \quad (5)$$

the reason for using the null-graph operator $\mathbf{T} \in \mathbb{R}^{n \times n}$ stems from the need to pay attention to certain geometric properties of the image's NS, which are extracted by \mathbf{L} . Let $\mathbf{T}\mathbf{x} = \mathbf{P}_n \mathbf{L} \mathbf{P}_n \mathbf{x} = \mathbf{P}_n \mathbf{L} \mathbf{x}_n$, where $\mathbf{L}\mathbf{x}_n$ extracts, areas of greatest difference in the NS, and then re-project it to the NS with \mathbf{P}_n , thus ensuring that this operation results in a projection from the NS. In Fig. 1, from left to right, we show the ground-truth \mathbf{x}^* , back-projection $\mathbf{H}^\top \mathbf{y}$, true null component $\mathbf{P}_n \mathbf{x}^*$, and two graph NS projections $\mathbf{P}_n \mathbf{L}_{8nn} \mathbf{P}_n \mathbf{x}^*$ and $\mathbf{P}_n \mathbf{L}_{4nn} \mathbf{P}_n \mathbf{x}^*$, for super-resolution (SR).



Figure 1. For image SR task with $SRF = 4$, $n = 3 \cdot 128^2$, we show ground-truth, adjoint reconstruction, NS projection, projection onto graph-smooth NS with \mathbf{L}_{4nn} and \mathbf{L}_{8nn} .

The map $\mathbf{P}_n \mathbf{x}^*$ isolates signal content invisible to the sensor, while $\mathbf{P}_n \mathbf{L} \mathbf{P}_n \mathbf{x}^*$ highlights where $\mathbf{L}\mathbf{x}_n$ falls into the NS. These graph projections highlight the smoothest *blind* signal components, e.g., textures near edges.

Then, by applying eigenvalue decomposition, we see that $\mathbf{T} = \mathbf{V} \text{diag}(\mu_1, \dots, \mu_n) \mathbf{V}^\top$ is SPSD, with $0 \leq \mu_1 \leq \dots \leq \mu_n$, where $\mathbf{V} \in \mathbb{R}^{n \times n}$ is orthogonal. Note that \mathbf{V} diagonalizes \mathbf{T} , so its columns $\{\mathbf{v}_i\}$ are the *graph-Fourier modes within* $\text{Null}(\mathbf{H})$. If μ_i is smaller, then a smoother graph-mode is selected. \mathbf{V} has the following properties: i) \mathbf{V} has orthonormal columns $\mathbf{v}_i \in \text{Null}(\mathbf{H})$, μ_i -ordered. ii) These $\{\mathbf{v}_i\}$ are *graph-smooth null modes* probing \mathbf{x} . The graph-smooth NS projector \mathbf{S} with p rows is obtained by taking the first p columns of \mathbf{V} :

$$\mathbf{S} = \overbrace{\mathbf{V}^\top}^{\mathbf{v}_p^\top}[:, 1:p]^\top = [\mathbf{v}_1, \dots, \mathbf{v}_p]^\top \in \mathbb{R}^{p \times n}. \quad (6)$$

Note that \mathbf{S} keeps only the p -smoothest null directions and $\mathbf{S}\mathbf{x}$ expresses the NS part of \mathbf{x} in an orthonormal basis sorted by increasing graph frequency. Particularly, based on RNSD: $\mathbf{S}\mathbf{x} = \mathbf{S}(\mathbf{P}_r + \mathbf{P}_n)\mathbf{x} = \mathbf{S}\mathbf{P}_r \mathbf{x} + \mathbf{S}\mathbf{P}_n \mathbf{x}$, since rows of \mathbf{S} lie in $\text{Null}(\mathbf{H})$, hence $\mathbf{S}\mathbf{P}_r = \mathbf{0}$, leading to

$$\mathbf{S}\mathbf{x} = \mathbf{0} + \mathbf{S}\mathbf{P}_n \mathbf{x} = \mathbf{V}_p^\top \mathbf{P}_n \mathbf{x} = \begin{bmatrix} \langle \mathbf{v}_1, \mathbf{x}_n \rangle \\ \vdots \\ \langle \mathbf{v}_p, \mathbf{x}_n \rangle \end{bmatrix}. \text{ Here } \{\mathbf{v}_i\}_{i=1}^p$$

are the p Laplacian-smoothest orthonormal null modes; thus $\mathbf{S}\mathbf{x}$ collects the coefficients of \mathbf{x} along these p directions.

3.3. Learning low-dimensional GSNR

We train the GSNR predictor \mathbf{G} following:

$$\mathbf{G}^* = \min_{\mathbf{G}} \mathbb{E}[\|\mathbf{G}(\mathbf{y}) - \mathbf{S}\mathbf{x}^*\|_2^2]. \quad (7)$$

Here, we aim to predict the low-dimensional GSNR using the neural network \mathbf{G} . Subsequently, the theoretical foundations will be laid that greater predictability will guarantee better convergence in the task.

3.4. Reconstruction objective

Thus, we incorporate our method as

$$\min_{\tilde{\mathbf{x}}} g(\tilde{\mathbf{x}}) + \lambda f(\tilde{\mathbf{x}}) + \gamma \|\mathbf{G}^*(\mathbf{y}) - \mathbf{S}\tilde{\mathbf{x}}\|_2^2 + \frac{\gamma_g}{2} \overbrace{\tilde{\mathbf{x}}^\top \mathbf{T} \tilde{\mathbf{x}}}^{\phi(\tilde{\mathbf{x}})}, \quad (8)$$

which includes the learned GSNR term, plus a graph regularizer acting only on the null component of the reconstruction, weighted by γ and γ_g , respectively. This retains compatibility with proximal/PnP/DM solvers.

4. Theory and Analysis

We develop a theoretical analysis on GSNR based on *null-restricted spectral* formulation that turns GSNR design/performance prediction into ordered-eigenvalue criteria on \mathbf{T} for optimal subspace selection, obtaining a principled eigen-ordering and criteria used to choose \mathbf{S} , p , \mathbf{L} . The theoretical results are summarized as:

Coverage: the first p eigenmodes of \mathbf{T} provide an optimal graph-smooth representation of $\text{Null}(\mathbf{H})$, by covering a high null-space spectrum energy with $p \ll n - m$.

Minimax optimality: the same GSNR basis is worst-case optimal over a graph-energy ellipsoid in $\text{Null}(\mathbf{H})$, giving a principled ordering of null directions

Predictability: via block-precision/Schur-complement analysis, we show that GSNR has a higher per-mode recoverability from measurements \mathbf{y} than plain null-space projections.

Convergence: the effect of the graph regularizer provides better conditioning and convergence properties based on fixed-point analysis.

4.1. Null-space coverage

Before developing the formal analysis on the coverage properties of the NS projections, we validate the representation performance of three settings: i) $\mathbf{L} = \mathbf{I}$, ii) \mathbf{L}_{4nn} , and iii) \mathbf{L}_{8nn} . Note that the first setting is equivalent to just taking the NS basis. In Fig. 2 (a), each row shows projections ($\mathbf{x} = (\mathbf{H}^T \mathbf{H} + \mathbf{S}^T \mathbf{S}) \mathbf{x}^*$) as the dimension of the null-space subspace increases, $p \in \{153, 1536, 4608, 9216, 15360\}$, for three graph choices in the design of \mathbf{S} : (top, orange) $\mathbf{L} = \mathbf{I}$; (middle, green) grid \mathbf{L}_{8nn} ; (bottom, blue) grid \mathbf{L}_{4nn} . For small p , the grid Laplacians already yield visually plausible faces, while $\mathbf{L} = \mathbf{I}$ still produces noisy, poorly structured estimates. The number printed above each image is the MSE of the representation. The plot at the bottom shows the MSE for all values of $p = \{1, \dots, n - m\}$, showing that the graph-null-space projections provide better signal representation with smaller p than just the NS basis. In general, to measure the amount of energy from the NS that the low-dimensional operator \mathbf{S} can capture, we use the spectral coverage defined as:

$$C(p) = \frac{\text{tr}(\mathbf{S} \text{Cov}(\mathbf{x}_n) \mathbf{S}^T)}{\text{tr}(\text{Cov}(\mathbf{x}_n))} \in [0, 1], \quad (9)$$

where $\text{Cov}(\mathbf{x})$ is the covariance matrix of \mathbf{x} . View the Laplacian eigenvectors as a graph-Fourier basis: the first modes are smooth, low “graph-frequency” patterns, while later modes are increasingly oscillatory [29, 42]. The $C(p)$ indicates what fraction of the total NS variance lies in the span of the first p graph-Fourier modes retained by \mathbf{S} , similarly as explained variance in PCA [18]. Intuitively, if the signal is graph-smooth, most variability concentrates in low

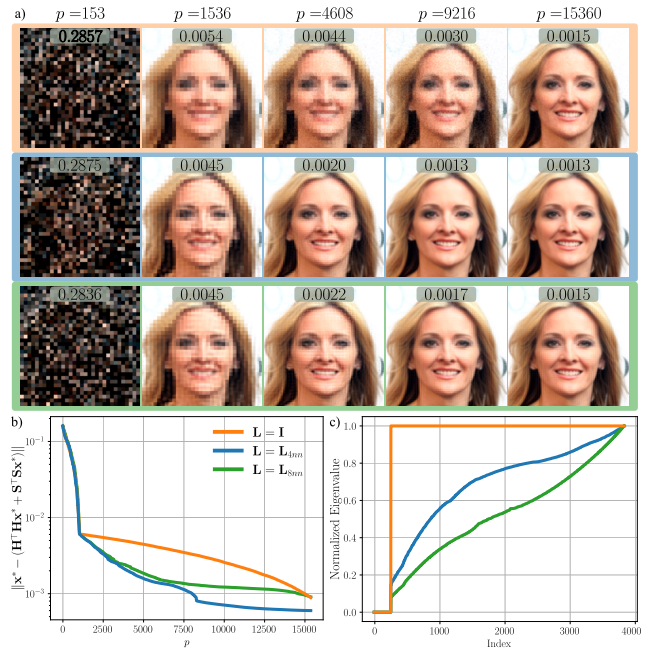


Figure 2. Coverage and spectral analysis for SR task. (a) $\mathbf{x}^* = \mathbf{H}^T \mathbf{H} \mathbf{x}^* + \mathbf{S}^T \mathbf{S} \mathbf{x}^*$ for \mathbf{S} given by (6) using $\mathbf{L} = \mathbf{I}$ (orange), $\mathbf{L} = \mathbf{L}_{4nn}$ (green) and $\mathbf{L} = \mathbf{L}_{8nn}$ (blue) for different values of p . (b) RNSD representation error, varying p . (c) Variation of \mathbf{T} normalized eigenvalues with respect to their index.

frequencies, so coverage climbs rapidly with small p ; if not, coverage grows more slowly, like in PCA. A4.2 shows coverage results and eigenvalue analysis that validate the usefulness of graph Laplacians, rather than a learnable matrix. Mathematical insights for the selection of the appropriate p value depending on the coverage are given in A5.

Definition 1 (Gaussian Markov Random Field [39]) A GMRF on the graph $\mathcal{G} = (\mathcal{V}, \mathcal{E})$ is a zero-mean Gaussian vector $\mathbf{x} \in \mathbb{R}^n$ with precision matrix $\mathbf{Q} = \boldsymbol{\Sigma}^{-1} \in \mathbb{R}^{n \times n}$, with $\boldsymbol{\Sigma} = \text{Cov}(\mathbf{x})$, is sparse and encodes the conditional independence of the graph

$$p(\mathbf{x}) \propto \exp\left(-\frac{1}{2} \mathbf{x}^T \mathbf{Q} \mathbf{x}\right), \quad \mathbf{Q}_{i,j} = 0 \iff (i, j) \notin \mathcal{E},$$

where smoothness is required in neighboring pixels, we define the precision matrix $\mathbf{Q} = \alpha \mathbf{L} + \epsilon \mathbf{I}$ with $\alpha > 0, \epsilon > 0$.

Under this setting, we derive the following guarantee on improved NS coverage.

Theorem 1 (Coverage for graph-smooth null-space)

Consider the construction of \mathbf{T} in (5). The covariance of the NS, $\text{Cov}(\mathbf{x}_n)$ is a spectral function of \mathbf{T} , i.e., $\text{Cov}(\mathbf{x}_n) = \mathbf{V} \text{diag}(\lambda_1, \dots, \lambda_n) \mathbf{V}^T$, where $\lambda_i = \frac{1}{\alpha \mu_i + \epsilon}$, $\lambda_1 \geq \lambda_2 \geq \dots \geq \lambda_n$. With the construction of \mathbf{S} in (6), the coverage of the NS using GMRF with a Laplacian matrix \mathbf{L} as $C_L(p)$ and the coverage when $\mathbf{L} = \mathbf{I}$ is denoted $C_I(p)$, satisfies for every $p = 1, \dots, n - m$.

$$C_L(p) \geq C_I(p).$$

The proof can be found in Supp. A1.

We illustrate this effect in Fig. 2(b)-(c). In 2(b), the representation error of the RNSD decreases more rapidly when using \mathbf{L}_{8nn} and \mathbf{L}_{4nn} compared to \mathbf{I} . In 2(c), the eigenvalue spectra of \mathbf{T} reveal that, unlike the flat spectrum of the pure NS projector \mathbf{P}_n , graph Laplacians exhibit smoothly increasing eigenvalues. From Theorem 1, a flat spectrum ($\mu_i = 1$ for all i as with $\mathbf{L} = \mathbf{I}$) yields $C_{\mathbf{I}}(p) = p/q$, so coverage grows only linearly with p , whereas Laplacians with increasing $\{\mu_i\}$ achieve faster coverage growth.

Our second theoretical result is a minimax optimality on the NS coverage by the NS scheme. First, define the feasible set of NS components

$$\mathcal{M}_\tau := \{\mathbf{x}_n \in \text{Null}(\mathbf{H}) : \mathbf{x}_n^\top \mathbf{L} \mathbf{x}_n \leq \tau\}$$

Theorem 2 (Minimax optimality) Let $V_p = \text{span}\{\mathbf{v}_1, \dots, \mathbf{v}_p\}$ and P_{V_p} be its projector. Then, among all p -dimensional $V \subset \text{Null}(\mathbf{H})$, provided $\mu_{p+1} > 0$,

$$\begin{aligned} \min_{\dim(V)=p} \sup_{\mathbf{x}_n \in \mathcal{M}_\tau} \|(\mathbf{I} - P_V)\mathbf{x}_n\|_2^2 &= \\ \sup_{\mathbf{x}_n \in \mathcal{M}_\tau} \|(\mathbf{I} - P_{V_p})\mathbf{x}_n\|_2^2 &= \frac{\tau}{\mu_{p+1}}. \end{aligned}$$

The proof of this theorem is in Supp. A2.

Remark 1 Selecting \mathbf{S} so that its rows are $\{\mathbf{v}_1^\top, \dots, \mathbf{v}_p^\top\}$ is provably optimal for covering the NS under the graph energy $\mathbf{x}^\top \mathbf{T} \mathbf{x}$. As p grows, the guaranteed worst-case error decays with $1/\mu_{p+1}$, which is fast for graph Laplacians (where many μ_j are small). With $\mathbf{L} = \mathbf{I}$ one gets $\mathbf{T} = \mathbf{P}_n$ (flat spectrum), hence $\mu_{p+1} = 1$ and no improvement in the bound, explaining why geometry-free designs cannot cover the NS efficiently.

4.2. Null-space projections predictability

It is also important to quantify the predictability level of the NS projections $\mathbf{S}\mathbf{x}^*$ from the acquired measurements \mathbf{y} . We develop a *statistical coupling* analysis via linear estimation.

Proposition 1 (Per-mode predictability bound) Let $\mathbf{x} \in \mathbb{R}^n$ be zero-mean Gaussian with covariance \mathbf{C} and precision $\mathbf{Q} = \mathbf{C}^{-1}$. Let $\mathbf{H} \in \mathbb{R}^{m \times n}$ and denote the orthogonal projectors onto $\mathcal{R} := \text{Range}(\mathbf{H}^\top)$ and $\mathcal{N} := \text{Null}(\mathbf{H})$ by \mathbf{P}_r and \mathbf{P}_n , respectively. Block \mathbf{Q} and \mathbf{C} with respect to the decomposition $\mathbb{R}^n = \mathcal{R} \oplus \mathcal{N}$:

$$\mathbf{Q} = \begin{bmatrix} \mathbf{Q}_{rr} & \mathbf{Q}_{rn} \\ \mathbf{Q}_{nr} & \mathbf{Q}_{nn} \end{bmatrix}, \quad \mathbf{C} = \begin{bmatrix} \mathbf{C}_{rr} & \mathbf{C}_{rn} \\ \mathbf{C}_{nr} & \mathbf{C}_{nn} \end{bmatrix}.$$

Assume $\mathbf{Q}_{nn} \succ 0$ on \mathcal{N} and let $\{\mathbf{v}_j\}$ be an orthonormal eigenbasis of \mathbf{Q}_{nn} with $\mathbf{Q}_{nn}\mathbf{v}_j = \mu_j \mathbf{v}_j$ and $\mu_j > 0$. Define the j -th null coefficient $a_j := \mathbf{v}_j^\top \mathbf{x}_n$ where $\mathbf{x}_n := \mathbf{P}_n \mathbf{x}$. Consider measurements from (1) and denote $\mathbf{C}_y := \mathbf{H}\mathbf{C}_{rr}\mathbf{H}^\top + \sigma^2 \mathbf{I}_m$. Then the population R^2 of the optimal linear predictor of a_j from \mathbf{y} satisfies

$$\begin{aligned} \rho_j^2 &:= \frac{\text{Cov}(a_j, \mathbf{y})^\top \mathbf{C}_y^{-1} \text{Cov}(\mathbf{y}, a_j)}{\text{Var}(a_j)} \leq \frac{c_j}{c_j + \mu_j}, \\ c_j &:= \mathbf{v}_j^\top (\mathbf{Q}_{rn} \mathbf{C}_{rr} \mathbf{Q}_{nr}) \mathbf{v}_j. \end{aligned}$$

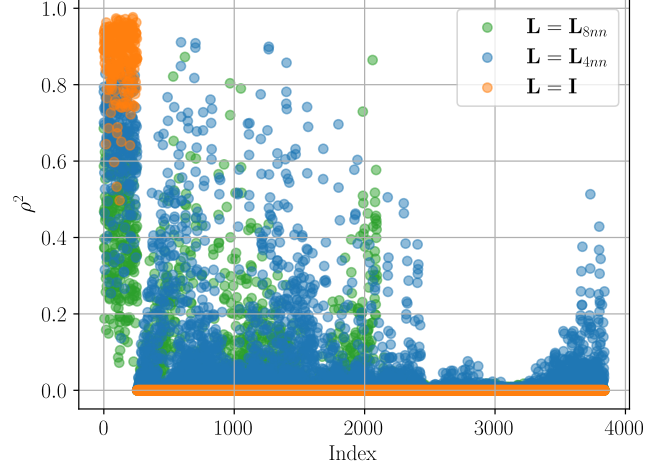


Figure 3. Per-mode predictability for each case when $\mathbf{L} \in \{\mathbf{I}, \mathbf{L}_{8nn}, \mathbf{L}_{4nn}\}$ for SR case with $SRF = 4$ with $n = 64^2$.

The proof of this proposition is found in Supp. A3.

Remark 2 If the prior is a GMRF with precision $\mathbf{Q} = \alpha \mathbf{L} + \varepsilon \mathbf{I}$ on \mathcal{L} , then $\mathbf{Q}_{nn} = \alpha \mathbf{T} + \varepsilon \mathbf{P}_n$ with $\mathbf{T} := \mathbf{P}_n \mathbf{L} \mathbf{P}_n$, and one can take $\{\mathbf{v}_j\}$ as the \mathbf{T} -eigenmodes (graph-smooth null modes). The bound becomes

$$\rho_j^2 \leq \frac{c_j}{c_j + \alpha \lambda_j(\mathbf{T}) + \varepsilon}, \quad c_j = \mathbf{v}_j^\top (\mathbf{Q}_{rn} \mathbf{C}_{rr} \mathbf{Q}_{nr}) \mathbf{v}_j,$$

with $\mathbf{Q}_{rn} = \alpha \mathbf{L}_{rn}$. Thus smoother null modes (small $\lambda_j(\mathbf{T})$) are more predictable. Now, if $\mathbf{L} = \mathbf{I}$ (isotropic prior), then $\mathbf{Q} = \gamma \mathbf{I}$ and $\mathbf{Q}_{rn} = \mathbf{P}_r \mathbf{Q} \mathbf{P}_n = \mathbf{0}$, so $c_j = 0$ and $\rho_j^2 \leq 0$ for all j : there is no statistical coupling between \mathcal{R} and \mathcal{N} .

To evaluate the developed theory, Fig. 3, the empirical per-mode predictability ρ_j^2 (one dot per eigenmode), for three choices of $\mathbf{L} \in \{\mathbf{L}_{8nn}, \mathbf{L}_{4nn}, \mathbf{I}\}$, where $\mathbf{L} = \mathbf{I}$ has same index ordering across panels. From indices $[0, m-1]$, the predictability is high for all settings, since they correspond to the eigenpairs related to the Range space, thus, the predictability is high. The observations are: (i) for $\mathbf{L} = \mathbf{I}$, the spectrum is constant over the NS and then drops to 0 outside of it, while both grid Laplacians exhibit a smooth, monotone growth of μ_j ; (ii) correspondingly, with grid Laplacians, a long tail of modes has non-zero predictability, (ρ_j^2 spread over a wide index range), whereas with $\mathbf{L} = \mathbf{I}$ only a small initial block of modes shows any predictability, and the rest are essentially 0. Note also that \mathbf{L}_{4nn} has higher predictability than \mathbf{L}_{8nn} in more eigenmodes, following the fast increase eigenvalue distribution Fig 2 (c).

Note that this analysis was using a linear estimation framework, harnessing the NS GMRF prior. In practice, the *statistical coupling* can also be achieved with the supervised learning of the predictor G in Eq. (7), but the trend of GS prior holds on this setting. To evaluate the predictability of the learned predictor, we used

$$R^2(p) \triangleq 1 - \frac{\mathbb{E} \left[\|\mathbf{G}^*(\mathbf{y}) - \mathbf{S}\mathbf{x}^*\|_2^2 \right]}{\mathbb{E} \left[\|\mathbf{S}\mathbf{x}^*\|_2^2 \right]}. \quad (10)$$

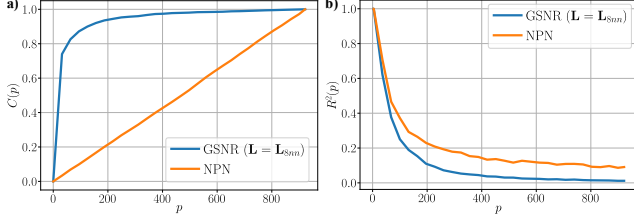


Figure 4. a) Coverage and b) Predictability vs. p for CS with CIFAR-10 dataset. In this case, $m/n = 0.1$ and $p = 1 \cdots n - m$.

4.3. Graph-based regularizer

Consider the PnP-PGD iteration solving the optimization problem (8) without the term $\|G^*(\mathbf{y}) - \mathbf{S}\mathbf{x}\|$ (for more detailed analysis of this term, see [17, Theorem 1]),

$$\mathbf{x}_{k+1} = D_\sigma(\mathbf{x}_k - \alpha(\nabla g(\mathbf{x}_k) + \gamma_g \nabla \phi(\mathbf{x}_k))) \quad (11)$$

$$= D_\sigma(\mathbf{x}_k - \alpha(\mathbf{H}^\top(\mathbf{H}\mathbf{x}_k - \mathbf{y}) + \gamma_g \mathbf{T}\mathbf{x}_k)), \quad (12)$$

where D_σ is a bounded denoiser with $\|D_\sigma(\mathbf{u}) - D_\sigma(\mathbf{v})\| \leq \sqrt{1 + \delta} \|\mathbf{u} - \mathbf{v}\|$ (as in [17, Assumption 2]), since $\nabla \phi(\mathbf{x}_k) = \mathbf{T}^\top \mathbf{x}_k = \mathbf{T}\mathbf{x}_k$. Let $\lambda_{\min} > 0$ and λ_{\max} be the extreme eigenvalues of $\mathbf{A}_{\gamma_g} = \mathbf{H}^\top \mathbf{H} + \gamma_g \mathbf{T}$ on $\text{span}(\text{Range}(\mathbf{H}^\top) \cup \text{Null}(\mathbf{H})) = \mathbb{R}^n$. Then for any step size $\alpha \in (0, 2/\lambda_{\max})$,

$$\|\mathbf{x}_{k+1} - \mathbf{x}^*\| \leq (1 + \delta) \|\mathbf{I} - \alpha \mathbf{A}_{\gamma_g}\|_2 \|\mathbf{x}_k - \mathbf{x}^*\| \quad (13)$$

$$\leq \rho \|\mathbf{x}_k - \mathbf{x}^*\|, \quad (14)$$

where $\rho = (1 + \delta) \max\{1 - \alpha \lambda_{\min}, \alpha \lambda_{\max} - 1\}$. In particular, if $\rho < 1$, The iteration is a contraction and converges linearly to a fixed point. The optimal α (for this linear bound) is $\alpha^* = \frac{2}{\lambda_{\min} + \lambda_{\max}}$ with rate $\rho^* = (1 + \delta) \frac{\kappa - 1}{\kappa + 1}$, $\kappa = \frac{\lambda_{\max}}{\lambda_{\min}}$. Compared with the baseline ($\gamma_g = 0$), adding $\gamma_g \mathbf{T}$: (i) makes $\mathbf{A}_{\gamma_g} \succ 0$ even on $\text{Null}(\mathbf{H})$, guaranteeing uniqueness of the quadratic subproblem, and (ii) reduces the condition number κ because \mathbf{T} acts precisely on directions where $\mathbf{H}^\top \mathbf{H}$ is small, improving convergence and ρ^* .

5. Experiments

To validate the proposed approach, we implemented it in PyTorch [31] and used the DeepInverse library [43] to benchmark different solvers, as detailed below. Since our work does not propose a specific network G , we validate the approach using a U-Net model [37] with a four-level 2D encoder-decoder architecture: the encoder applies double convolution blocks with $C, 2C, 4C$, and $8C$ channels (with $C = 64$) and 2×2 max-pooling, while the decoder uses nearest-neighbor upsampling with skip connections, refining features back to C channels before a final 1×1 convolution produces the output. The network is optimized using the Adam optimizer [21] with a learning rate of 10^{-3} for 50 epochs. For all experiments, we used a noise variance $\sigma^2 = 0.05$. Code at ¹. We consider the inverse problems:

¹github.com/yromariogh/GSNR

Compressed Sensing (CS): $\mathbf{H} \in \{-1, 1\}^{m \times n}$ are the first 10% rows of a Hadamard matrix $\mathbf{A} \in \{-1, 1\}^{n \times n}$ [5]. We validate with CIFAR-10 [23] and CelebA [25] datasets.

Super-Resolution (SR): We set $n = 3 \cdot 128^2$ and use an SR factor (SRF) of 4, i.e., $m = 3 \cdot 32^2$. We validate on the CelebA dataset [25], using 10000 training images resized to 128×128 . We also show results for the Synthetic Aperture Radar (SAR) image dataset [11].

Demosaicing: We used the CelebA dataset, resized to 64×64 , and the Bayer filter [3] acquisition pattern.

Deblurring: We set $n = 64^2 \cdot 3$ and used a 2-D Gaussian kernel with a bandwidth $\sigma_k = 1$. We validated our experiments on the CelebA [25] dataset and the Places365 [54] dataset, both resized to 64×64 , using 10000 images for training and a batch size of 32.

For all of these imaging tasks, we construct the null-restricted Laplacian \mathbf{T} and the matrix \mathbf{S} , leveraging properties of \mathbf{H} . Details on the computation of these matrices in A5. We provide comprehensive ablations of GSNR in A6.

5.1. Predictability and Coverage

The coverage definition in (9), has a general expression for the covariance matrix computation. In practice, we computed as follows. Given centered images \mathbf{x}_i and their null projections $\mathbf{x}_{n,i} = \mathbf{P}_n(\mathbf{x}_i - \bar{\mathbf{x}})$, where $\bar{\mathbf{x}} = \frac{1}{N} \sum_{i=1}^N \mathbf{x}_i$ and the NS covariance $\text{Cov}(\mathbf{x}_n) = \frac{1}{N} \sum_{i=1}^N \mathbf{x}_{n,i} \mathbf{x}_{n,i}^\top$. Fig. 4 shows the results in terms of (a) Coverage and (b) Predictability in CS for different operators \mathbf{S} , under the same acquisition matrix \mathbf{H} . We used the $N = 10000$ image of the CIFAR-10 dataset. In this case, NPN ($\mathbf{L} = \mathbf{I}$) is obtained following [17, Eq. 3], and GSNR uses $\mathbf{L} = \mathbf{L}_{8nm}$. Note that here we take the first p rows of each \mathbf{S} . Supp. A9 shows additional results for CS. A7 shows the coverage curves for the SR task.

5.2. Diffusion Solvers

We used two diffusion model (DM) solvers, DPS [8] and DiffPIR [55]. See Supp. A8 for more details on the adaptation of these models with the proposed approach. Fig. 5 compares DPS and DiffPIR with and without the proposed GSNR term. In all cases, the baseline DM already produces plausible faces, but it often leaves residual blur and aliasing around high-frequency structures such as hair, eyebrows, and facial contours. When we replace the generic NS basis by the GSNR, the reconstructions become visibly sharper and more faithful to the ground truth: edges around the jawline and nose are better defined, textures are less washed out, and blocky artifacts from the low-resolution observation \mathbf{y} are further suppressed. These qualitative improvements are consistent with the quantitative SSIM/P-SNR numbers printed in each panel: the gains over the baseline DiffPIR/DPS are modest in dB but systematic (e.g., $30.19 \rightarrow 30.31$; $30.19 \rightarrow 30.48$), indicating that the GSNR term helps the diffusion prior resolve NS ambiguities rather than hallucinating arbitrary details. In other words, the DM

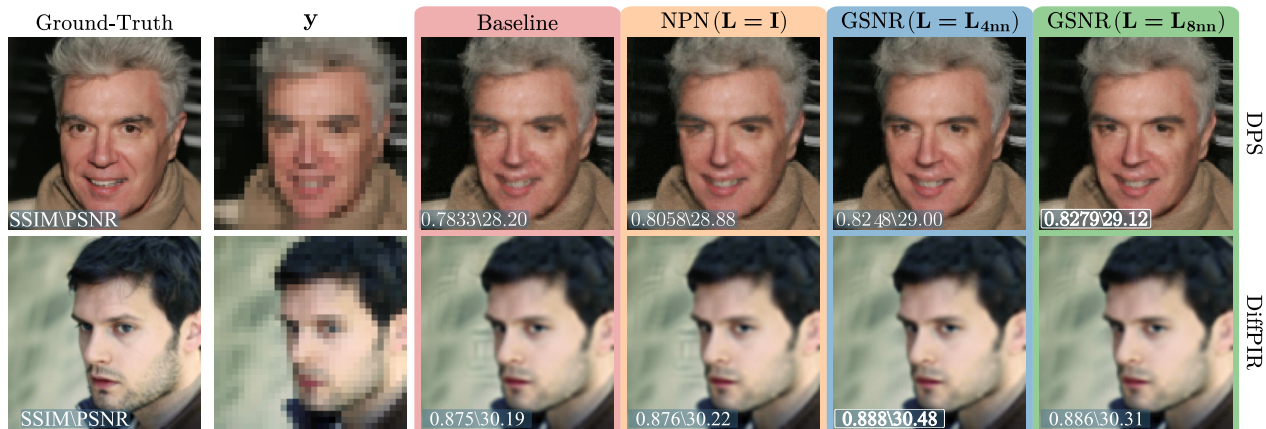


Figure 5. Results of DM-based solvers (DPS [8] & DiffPIR [55]) for Baseline, NPN [17], and GSNR with L_{4nn} and L_{8nn} . Here, $p = 0.1n$.

Table 1. Quantitative comparison on the super-resolution and demosaicing tasks (higher is better) using the CelebA test set. For each task, the **best** result and **second-best** results.

Method	Task	
	Super-Resolution	Demosaicing
PnP [20]	27.37	39.35
NPN [17]	29.21	39.77
DDN-Cascade [7]	28.92	37.83
DDN-Independent [7]	28.81	38.92
DNSN [41]	26.52	39.33
Unrolling [50]	28.97	38.82
GSNR-PnP w. L_{8nn}	29.38	39.88
GSNR-PnP w. L_{4nn}	29.42	39.89

still provides the powerful image prior, but GSNR steers it along graph-smooth NS directions that are predictable from y and compatible with the forward model, yielding more accurate and stable reconstructions. Supp. A8 shows the integration of GSNR in latent-space DMs [15].

5.3. Comparison with End-to-End Methods

Table 1 reports PSNR on SR and demosaicing, comparing classical PnP, the proposed GSNR-PnP variants, NPN, and several strong deep-learning baselines. Across both tasks, GSNR-PnP with graph Laplacians L_{4nn} and L_{8nn} achieves the best performance. For SR, GSNR-PnP yields roughly a 2 dB gain over vanilla PGD-PnP and a clear margin over both NPN (with $L = I$) and task-specific unrolled/cascade architectures. For demosaicing, the problem is less ill-posed, so the absolute gains are smaller, but GSNR-PnP still provides a consistent improvement over PGD-PnP, NPN, and the deep baselines. Overall, these results show that injecting graph-smooth NS structure into a standard PnP solver consistently improves upon (i) geometry-free PnP/NPN baselines and (ii) specialized deep unrolled or cascade architectures, with particularly strong benefits on the most underdetermined SR task. In A10 and A11, we show additional results for Demosaicing and SR, respectively.

Table 2. Final PSNR (dB) for deblurring ($\sigma_k = 1$) with $n = 64^2 \cdot 3$ and $p = 0.8 \cdot n$. We report results on Places365 [11] and CelebA [25] test sets using Lip-DnCNN [40] and a wavelet denoiser [12]. For each column, **best** and **second-best** results.

Method	γ_g	Places365		CelebA	
		Lip-DnCNN	Wavelet	Lip-DnCNN	Wavelet
Baseline (PGD-PnP)	–	31.58	30.78	35.26	33.64
NPN [17]	–	33.22	33.17	37.86	37.68
GSNR w. L_{8nn}	✗	33.60	33.59	38.18	37.99
GSNR w. L_{4nn}	✓	33.60	33.59	38.18	37.99

5.4. Plug-and-Play

We used the PGD-PnP [16, 20], but GSNR can be easily adapted to other formulations, such as ADMM [6] or HQS [33]. We used three denoisers: DnCNN with Lipchitz training (Lip-DnCNN) [40], DRUNet [52], Wavelet denoiser (Daubechies 8 with 4 levels) using soft-thresholding proximal [12]. For improving stability and performance of the PGD-PnP, we include the equivariant denoising technique [45] with two random 90 rotations and two reflections.

Deblurring: Table 2 reports the final PSNR for deblurring on Places365 and CelebA under different graph variants and denoisers. In all settings, both NPN and GSNR substantially improve over the baseline PGD-PnP solver: on CelebA, the gain is on the order of +2 dB for both Lip-DnCNN and the wavelet denoiser, and on Places365, the gain is around +1.5–2 dB. The GSNR variant with L_{8nn} provides a small but consistent improvement over NPN on both datasets and for both denoisers, indicating that injecting NS structure into the NS helps the solver recover sharper details without overfitting. Interestingly, turning the additional graph penalty on or off (γ_g ✓ vs. ✗) has a negligible effect on the final PSNR in this experiment, suggesting that the learned GSNR already captures most of the useful graph structure for deblurring. Figure 6 shows the deblurring convergence behaviour with the DnCNN denoiser. The baseline PnP-PGD curve increases steadily but saturates at a lower PSNR plateau. In contrast, both GSNR variants (with $\gamma_g = 0$ and $\gamma_g = 0.1$) converge to a noticeably higher final PSNR, confirming that the graph-smooth null-space repre-

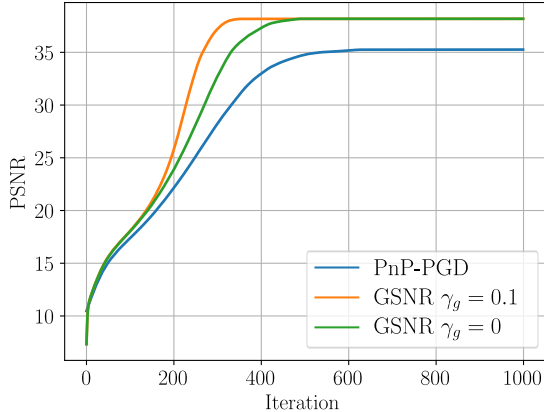


Figure 6. Deblurring convergence curves for PnP-PGD baseline using Lip-DnCNN and GSNR variants with L_{8nn} with and without the null-restricted Laplacian regularization.

sensation improves the fixed point of the algorithm. The explicit null-only graph penalty ($\gamma_g = 0.1$) mainly affects the transient regime: it accelerates convergence in the first few hundred iterations, reaching near-peak PSNR significantly earlier than GSNR with $\gamma_g = 0$ (aligned with the theoretical analysis conducted in Sec. 4.3), while all three methods eventually stabilize. Additional visual results in A12.

SR: Fig. 7 shows an SR example for different graph designs and denoisers. Columns correspond to the choice of Laplacian L or to the baseline PnP without GSNR, while rows correspond to different denoisers. In all three rows, moving from the baseline and $L = I$ columns to the graph-based L_{4nn} and L_{8nn} columns produces visibly sharper details: facial contours are crisper, hair strands are better resolved, and blocky artifacts inherited from the low-resolution backprojection $H^T y$ are reduced. The improvements are most pronounced for the DnCNN and DRUNet denoisers. Still, they are also clearly present for the simpler Wavelet denoiser, indicating that the benefit comes from the GSNR itself rather than from the denoiser. Among the graph designs, L_{8nn} yields the visually clearest reconstruction, suggesting that richer graph connectivity enables the solver to exploit structure in the null space rather than hallucinating high-frequency content. Results with Deep Image Prior [49] and SAR images in SR can be found in A11.

6. Discussion

We demonstrate that GSNR is a versatile approach for a broad range of inverse problems, data modalities, and neural networks (A14). Nevertheless, the method requires precise knowledge of the sensing matrix, which is unavailable in some applications, e.g., real-world image deblurring. In A15, we provide analysis on the effect of uncertainty in the sensing operator, where a performance drop is evident, but the improvement compared with the baseline algorithm is maintained. Follow-up ideas will harness the null-space construction under sensing matrix uncertainty for calibrated null-space regularization functions. Another aspect

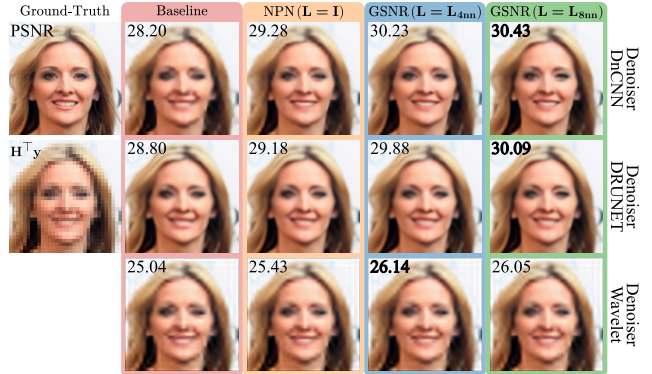


Figure 7. Results of PnP, NPN, and GSNR varying L and denoisers. Best results for each denoiser are in bold. Here, $p = 0.1n$.

of GSNR is the requirement to perform EVD on the null-restricted Laplacian T , which, at large image scales, necessitates substantial computational resources. However, this computation is performed *offline* once per (H, L, n, p) , and reused for learning the network G and the reconstruction step. In A13, we provide a detailed runtime analysis of the approach. Additionally, our approach is designed for linear inverse problems; the adaptation for nonlinear inverse problems, e.g., phase retrieval, requires careful modeling of the invertibility properties of the sensing operator and its input-dependent ambiguities. In recent work [14], a generalization of the null-space property was developed for neural networks (non-linear functions), opening new frontiers for learning optimal null-space components.

7. Conclusion and Future Outlook

We introduced *GSNR: Graph-Smooth Null-Space Representation*, which equips an inverse problem solver not only with *what* the measurements constrain, but also with *how* to use the degrees of freedom that the sensor never sees (null-space). Instead of regularizing the full image, GSNR builds a low-dimensional basis for $\text{Null}(H)$ aligned with graph smoothness via the null-restricted Laplacian $T = P_n L P_n$, and can optionally add a null-only graph penalty at inference. Theoretically, the smoothest T -modes are minimax-optimal for null-space components, and under a GMRF prior, they provably capture more null-space variance than geometry-free choices while enjoying stronger statistical coupling to the measurements. In practice, this yields better coverage of plausible solutions, higher predictability of null-space signal components, and improved conditioning, translating into faster and more stable convergence of PnP and diffusion-based solvers. Looking ahead, rather than fixing L to a hand-crafted grid Laplacian, learning the graph structure or employing interpretable graph neural operators promises data-adaptive GSNR bases that better reflect semantic structure. Also, a more rigorous study of GSNR within generative solvers could provide a principled way to inject graph-smooth null constraints into these frameworks without breaking their probabilistic interpretation.

References

- [1] Eirikur Agustsson and Radu Timofte. Ntire 2017 challenge on single image super-resolution: Dataset and study. In *The IEEE Conference on Computer Vision and Pattern Recognition (CVPR) Workshops*, 2017. 11
- [2] Daniel Otero Baguer, Johannes Leuschner, and Maximilian Schmidt. Computed tomography reconstruction using deep image prior and learned reconstruction methods. *Inverse Problems*, 36(9):094004, 2020. 1
- [3] Bryce E Bayer. Color imaging array, 1976. US Patent 3,971,065. 6
- [4] Martin Benning and Martin Burger. Modern regularization methods for inverse problems. *Acta numerica*, 27:1–111, 2018. 1
- [5] E. J. Candes and M. B. Wakin. An introduction to compressive sampling. *IEEE Signal Processing Magazine*, 25(2):21–30, 2008. 1, 6
- [6] Stanley H Chan, Xiran Wang, and Omar A Elgendy. Plug-and-play admm for image restoration: Fixed-point convergence and applications. *IEEE Transactions on Computational Imaging*, 3(1):84–98, 2016. 1, 7
- [7] Dongdong Chen and Mike E Davies. Deep decomposition learning for inverse imaging problems. In *Computer Vision–ECCV 2020: 16th European Conference, Glasgow, UK, August 23–28, 2020, Proceedings, Part XXVIII 16*, pages 510–526. Springer, 2020. 2, 7
- [8] Hyungjin Chung, Jeongsol Kim, Michael Thompson McCann, Marc Louis Klasky, and Jong Chul Ye. Diffusion posterior sampling for general noisy inverse problems. In *The Eleventh International Conference on Learning Representations*, 2023. 6, 7, 1
- [9] Regev Cohen, Michael Elad, and Peyman Milanfar. Regularization by denoising via fixed-point projection (red-pro). *SIAM Journal on Imaging Sciences*, 14(3):1374–1406, 2021. 1
- [10] Yuning Cui, Syed Waqas Zamir, Salman Khan, Alois Knoll, Mubarak Shah, and Fahad Shahbaz Khan. Adair: Adaptive all-in-one image restoration via frequency mining and modulation. In *13th international conference on learning representations, ICLR 2025*, pages 57335–57356. International Conference on Learning Representations, ICLR, 2025. 11
- [11] Emanuele Dalsasso, Xiangli Yang, Loic Denis, Florence Tupin, and Wen Yang. Sar image despeckling by deep neural networks: From a pre-trained model to an end-to-end training strategy. *Remote Sensing*, 12(16):2636, 2020. 6, 7
- [12] David L Donoho. De-noising by soft-thresholding. *IEEE transactions on information theory*, 41(3):613–627, 2002. 7
- [13] David L Donoho and Iain M Johnstone. Ideal spatial adaptation by wavelet shrinkage. *Biometrika*, 81(3):425–455, 1994. 2
- [14] Yamit Ehrlich, Nimrod Berman, and Assaf Shocher. Pseudo-invertible neural networks. *arXiv preprint arXiv:2602.06042*, 2026. 8
- [15] Yutong He, Naoki Murata, Chieh-Hsin Lai, Yuhta Takida, Toshimitsu Uesaka, Dongjun Kim, Wei-Hsiang Liao, Yuki Mitsufuji, J Zico Kolter, Ruslan Salakhutdinov, and Stefano Ermon. Manifold preserving guided diffusion. In *The Twelfth International Conference on Learning Representations*, 2024. 7, 1, 8
- [16] Samuel Hurault, Antonin Chambolle, Arthur Leclaire, and Nicolas Papadakis. A relaxed proximal gradient descent algorithm for convergent plug-and-play with proximal denoiser. In *International Conference on Scale Space and Variational Methods in Computer Vision*, pages 379–392. Springer, 2023. 7
- [17] Roman Jacome, Romario Gualdrón-Hurtado, León Suárez-Rodríguez, and Henry Arguello. NPN: Non-Linear Projections of the Null-Space for Imaging Inverse Problems. In *The Thirty-ninth Annual Conference on Neural Information Processing Systems*, 2025. 2, 6, 7, 9, 11
- [18] Ian T Jolliffe and Jorge Cadima. Principal component analysis: a review and recent developments. *Philosophical transactions of the royal society A: Mathematical, Physical and Engineering Sciences*, 374(2065):20150202, 2016. 4
- [19] Vassilis Kalofolias. How to learn a graph from smooth signals. In *Artificial intelligence and statistics*, pages 920–929. PMLR, 2016. 2
- [20] Ulugbek S. Kamilov, Charles A. Bouman, Gregory T. Buzard, and Brendt Wohlberg. Plug-and-play methods for integrating physical and learned models in computational imaging: Theory, algorithms, and applications. *IEEE Signal Processing Magazine*, 40(1):85–97, 2023. 1, 2, 7
- [21] Diederik P Kingma and Jimmy Ba. Adam: A method for stochastic optimization. *arXiv preprint arXiv:1412.6980*, 2014. 6
- [22] Lingshun Kong, Jiangxin Dong, Jinhui Tang, Ming-Hsuan Yang, and Jinshan Pan. Efficient visual state space model for image deblurring. In *Proceedings of the computer vision and pattern recognition conference*, pages 12710–12719, 2025. 11
- [23] Alex Krizhevsky. Learning multiple layers of features from tiny images. 2009. 6
- [24] Richard B Lehoucq, Danny C Sorensen, and Chao Yang. *ARPACK users’ guide: solution of large-scale eigenvalue problems with implicitly restarted Arnoldi methods*. SIAM, 1998. 4
- [25] Ziwei Liu, Ping Luo, Xiaogang Wang, and Xiaoou Tang. Deep learning face attributes in the wild. In *Proceedings of International Conference on Computer Vision (ICCV)*, 2015. 6, 7
- [26] Michael Lustig, David L Donoho, Juan M Santos, and John M Pauly. Compressed sensing mri. *IEEE signal processing magazine*, 25(2):72–82, 2008. 1
- [27] Peyman Milanfar and Mauricio Delbracio. Denoising: a powerful building block for imaging, inverse problems and machine learning. *Philosophical Transactions A*, 383(2299):20240326, 2025. 1
- [28] Sunil K Narang, Yung Hsuan Chao, and Antonio Ortega. Graph-wavelet filterbanks for edge-aware image processing. In *2012 IEEE Statistical Signal Processing Workshop (SSP)*, pages 141–144, 2012. 2
- [29] Antonio Ortega, Pascal Frossard, Jelena Kovačević, José MF Moura, and Pierre Vandergheynst. Graph signal processing: Overview, challenges, and applications. *Proceedings of the IEEE*, 106(5):808–828, 2018. 2, 3, 4

- [30] Neal Parikh and Stephen Boyd. Proximal algorithms. *Found. Trends Optim.*, 1(3):127–239, 2014. 2
- [31] Adam Paszke, Sam Gross, Francisco Massa, Adam Lerer, James Bradbury, Gregory Chanan, Trevor Killeen, Zeming Lin, Natalia Gimelshein, Luca Antiga, Alban Desmaison, Andreas Köpf, Edward Yang, Zach DeVito, Martin Raison, Alykhan Tejani, Sasank Chilamkurthy, Benoit Steiner, Lu Fang, Junjie Bai, and Soumith Chintala. *PyTorch: an imperative style, high-performance deep learning library*. Curran Associates Inc., Red Hook, NY, USA, 2019. 6
- [32] Gabriel Peyré, Sébastien Bougleux, and Laurent Cohen. Non-local regularization of inverse problems. In *Computer Vision – ECCV 2008*, pages 57–68, Berlin, Heidelberg, 2008. Springer Berlin Heidelberg. 2
- [33] Arash Rasti-Meymandi, Aboozar Ghaffari, and Emad Fatemizadeh. Plug and play augmented hqs: Convergence analysis and its application in mri reconstruction. *Neuro-computing*, 518:1–14, 2023. 7
- [34] Edward T Reehorst and Philip Schniter. Regularization by denoising: Clarifications and new interpretations. *IEEE transactions on computational imaging*, 5(1):52–67, 2018. 1
- [35] Yaniv Romano, Michael Elad, and Peyman Milanfar. The little engine that could: Regularization by denoising (red). *SIAM journal on imaging sciences*, 10(4):1804–1844, 2017. 1, 2
- [36] Robin Rombach, Andreas Blattmann, Dominik Lorenz, Patrick Esser, and Björn Ommer. High-resolution image synthesis with latent diffusion models. In *Proceedings of the IEEE/CVF conference on computer vision and pattern recognition*, pages 10684–10695, 2022. 8
- [37] Olaf Ronneberger, Philipp Fischer, and Thomas Brox. U-net: Convolutional networks for biomedical image segmentation. In *International Conference on Medical image computing and computer-assisted intervention*, pages 234–241. Springer, 2015. 6
- [38] Leonid I. Rudin, Stanley Osher, and Emad Fatemi. Nonlinear total variation based noise removal algorithms. *Physica D: Nonlinear Phenomena*, 60(1):259–268, 1992. 2
- [39] Havarad Rue and Leonhard Held. *Gaussian Markov random fields: theory and applications*. Chapman and Hall/CRC, 2005. 4
- [40] Ernest Ryu, Jialin Liu, Sicheng Wang, Xiaohan Chen, Zhangyang Wang, and Wotao Yin. Plug-and-play methods provably converge with properly trained denoisers. In *International Conference on Machine Learning*, pages 5546–5557. PMLR, 2019. 7, 9
- [41] Johannes Schwab, Stephan Antholzer, and Markus Haltmeier. Deep null space learning for inverse problems: convergence analysis and rates. *Inverse Problems*, 35(2):025008, 2019. 2, 7
- [42] David I Shuman, Sunil K Narang, Pascal Frossard, Antonio Ortega, and Pierre Vandergheynst. The emerging field of signal processing on graphs: Extending high-dimensional data analysis to networks and other irregular domains. *IEEE signal processing magazine*, 30(3):83–98, 2013. 3, 4
- [43] Julián Tachella, Matthieu Terris, Samuel Hurault, Andrew Wang, Leo Davy, Jérémy Scanvic, Victor Sechaud, Romain Vo, Thomas Moreau, Thomas Davies, Dongdong Chen, Nils Laurent, Brayan Monroy, Jonathan Dong, Zhiyuan Hu, Minh-Hai Nguyen, Florian Sarron, Pierre Weiss, Paul Escande, Mathurin Massias, Thibaut Modrzyk, Brett Levac, Tobías I. Liaudat, Maxime Song, Johannes Hertrich, Sebastian Neumayer, and Georg Schramm. Deepinverse: A python package for solving imaging inverse problems with deep learning. *Journal of Open Source Software*, 10(115):8923, 2025. 6
- [44] Hong Ye Tan, Subhadip Mukherjee, and Junqi Tang. From image denoisers to regularizing imaging inverse problems: An overview. *arXiv preprint arXiv:2509.03475*, 2025. 1
- [45] Matthieu Terris, Thomas Moreau, Nelly Pustelnik, and Julian Tachella. Equivariant plug-and-play image reconstruction. In *Proceedings of the IEEE/CVF Conference on Computer Vision and Pattern Recognition*, pages 25255–25264, 2024. 7
- [46] Jing Tian and Kai-Kuang Ma. A survey on super-resolution imaging. *Signal, Image and Video Processing*, 5:329–342, 2011. 1
- [47] Xiangpeng Tian, Xiangyu Liao, Xiao Liu, Meng Li, and Chao Ren. Degradation-aware feature perturbation for all-in-one image restoration. In *Proceedings of the IEEE/CVF Conference on Computer Vision and Pattern Recognition*, pages 28165–28175, 2025. 11
- [48] Singanallur V. Venkatakrishnan, Charles A. Bouman, and Brendt Wohlberg. Plug-and-play priors for model based reconstruction. In *2013 IEEE Global Conference on Signal and Information Processing*, pages 945–948, 2013. 1
- [49] Lizhi Wang, Chen Sun, Ying Fu, Min H Kim, and Hua Huang. Hyperspectral image reconstruction using a deep spatial-spectral prior. In *Proceedings of the IEEE/CVF Conference on Computer Vision and Pattern Recognition*, pages 8032–8041, 2019. 8
- [50] Jinxi Xiang, Yonggui Dong, and Yunjie Yang. Fista-net: Learning a fast iterative shrinkage thresholding network for inverse problems in imaging. *IEEE Transactions on Medical Imaging*, 40(5):1329–1339, 2021. 7
- [51] Jiahui Yu, Zhe Lin, Jimei Yang, Xiaohui Shen, Xin Lu, and Thomas S Huang. Generative image inpainting with contextual attention. In *Proceedings of the IEEE conference on computer vision and pattern recognition*, pages 5505–5514, 2018. 1
- [52] Kai Zhang, Yawei Li, Wangmeng Zuo, Lei Zhang, Luc Van Gool, and Radu Timofte. Plug-and-play image restoration with deep denoiser prior. *IEEE Transactions on Pattern Analysis and Machine Intelligence*, 44(10):6360–6376, 2021. 1, 7, 9
- [53] Kaihao Zhang, Wenqi Ren, Wenhan Luo, Wei-Sheng Lai, Björn Stenger, Ming-Hsuan Yang, and Hongdong Li. Deep image deblurring: A survey. *International Journal of Computer Vision*, 130(9):2103–2130, 2022. 1
- [54] Bolei Zhou, Agata Lapedriza, Aditya Khosla, Aude Oliva, and Antonio Torralba. Places: A 10 million image database for scene recognition. *IEEE Transactions on Pattern Analysis and Machine Intelligence*, 2017. 6

- [55] Yuanzhi Zhu, Kai Zhang, Jingyun Liang, Jiezhang Cao, Bihan Wen, Radu Timofte, and Luc Van Gool. Denoising diffusion models for plug-and-play image restoration. In *Proceedings of the IEEE/CVF Conference on Computer Vision and Pattern Recognition (CVPR) Workshops*, pages 1219–1229, 2023. [6](#), [7](#), [1](#), [8](#)

GSNR: Graph Smooth Null-Space Representation for Inverse Problems

Supplementary Material

Appendix Contents

A1 . Proof of Theorem 1	1
A2 . Proof of Theorem 2	2
A3 . Proof of Proposition 1	2
A4 . Graph structures	3
A4.1. Additional graphs	3
A4.2 Learning a Structured Laplacian	4
A5 . Settings for construction null-restricted Laplacian in practice	4
A6 . Ablation Studies of the Graph Regularizer	5
A6.1. Why graph smooth null-space?	5
A6.2 Why low-dimensional null-space projections?	6
A6.3 Cost-function ablation	6
A6.4 Minimax optimality bound	6
A6.5 Fixed-point convergence	7
A7 . Coverage curve	7
A8 . GSNR inclusion in Diffusion-based solvers	7
A8.1 DPS [8].	7
A8.2 DiffPIR [55].	8
A8.3 MPGD [15].	8
A9 . CS results	9
A10. Demosaicking results	9
A11. SR results	9
A12 Deblurring results	10
A13 Scalability and computational cost	11
A14 Dataset generalization and neural network ablation	11
A15. Inexact forward operator	12
A1. Proof of Theorem 1	

Theorem 1 (Coverage for graph smooth null-space)
 Consider the construction of \mathbf{T} Eq (5), the covariance of the null-space $\text{Cov}(\mathbf{x}_n)$ is a spectral function of \mathbf{T} , i.e., $\text{Cov}(\mathbf{x}_n) = \mathbf{V} \text{diag}(\lambda_1, \dots, \lambda_q) \mathbf{V}^\top$, where $\lambda_i = \frac{1}{\alpha \mu_i + \epsilon}$, $\lambda_1 \geq \lambda_2 \geq \dots \geq \lambda_q$. With the construction of \mathbf{S} in (6), the coverage of the null-space using GMRF with a Laplacian

matrix \mathbf{L} as $C_L(p)$ and the coverage when $\mathbf{L} = \mathbf{I}$ is denoted $C_I(p)$, satisfies for every $p = 1, \dots, q$

$$C_L(p) \geq C_I(p) \quad (15)$$

Using cyclicity of the trace and $P(p) = \mathbf{V}_p \mathbf{V}_p^\top$,

$$\begin{aligned} \text{tr}(P(p) \text{Cov}) &= \text{tr}(\mathbf{V}_p \mathbf{V}_p^\top \mathbf{V} \text{diag}(\lambda) \mathbf{V}^\top) \\ &= \text{tr}((\mathbf{V}^\top \mathbf{V}_p)(\mathbf{V}^\top \mathbf{V}_p)^\top \text{diag}(\lambda)) \\ &= \text{tr}(\text{diag}(\lambda_1, \dots, \lambda_p)) = \sum_{i=1}^p \lambda_i. \end{aligned}$$

Also $\text{tr}(\text{Cov}) = \sum_{i=1}^q \lambda_i$. Hence

$$C_L(p) = \frac{\sum_{i=1}^p \lambda_i}{\sum_{i=1}^q \lambda_i}. \quad (16)$$

Consider the case $\mathbf{L} = \mathbf{I} \rightarrow \mathbf{T} = \mathbf{P}_n$ due to the symmetric and idempotent property of the null-space projector. Any symmetric and idempotent matrix is diagonalizable with eigenvalues only in $\{0, 1\}$. Then, any eigenvector and eigenvalue pair $(\mathbf{v}_i, \lambda_i)$ satisfy

$$\lambda_i = \begin{cases} 1, & \text{if } \mathbf{v}_i \in \text{Null}(\mathbf{H}), \\ 0, & \text{if } \mathbf{v}_i \in \text{Range}(\mathbf{H}^\top). \end{cases}$$

Under this analysis, replacing the eigenvalues λ_i in (16), we have

$$C_I(p) = \frac{p}{q}. \quad (17)$$

Since (λ_i) is nonincreasing, the mean of the first p terms is at least the global mean:

$$\frac{1}{p} \sum_{i=1}^p \lambda_i \geq \frac{1}{q} \sum_{i=1}^q \lambda_i \iff \frac{\sum_{i=1}^p \lambda_i}{\sum_{i=1}^q \lambda_i} \geq \frac{p}{q}.$$

Combining with (16)–(17) gives $C_L(p) \geq C_I(p)$ for all p , with strict inequality whenever (λ_i) is not constant.

Corollary 1 Using $\lambda_i = \frac{1}{\alpha \mu_i + \epsilon}$, $\mu_1 \leq \dots \leq \mu_q$, and the bounds $\sum_{i \leq p} \lambda_i \geq p \lambda_p$ and $\sum_{i \leq q} \lambda_i \leq p \lambda_1 + (q - p) \lambda_{p+1}$, we obtain

$$C_L(p) \geq \frac{p \lambda_p}{p \lambda_1 + (q - p) \lambda_{p+1}} \quad (18)$$

$$= \frac{1}{\frac{\alpha \mu_p + \epsilon}{\alpha \mu_1 + \epsilon} + \frac{q-p}{p} \frac{\alpha \mu_p + \epsilon}{\alpha \mu_{p+1} + \epsilon}} \geq \frac{p}{q}, \quad (19)$$

with the last inequality again strict unless the spectrum is flat. This makes explicit how fast coverage rises for Laplacians whose $\{\mu_i\}$ increase rapidly (grids/graphs) compared to $\mathbf{L} = \mathbf{I}$.

A2. Proof of Theorem 2

Theorem 2 (Minimax optimality) Let $V_p = \text{span}\{\mathbf{v}_1, \dots, \mathbf{v}_p\}$ and P_{V_p} be its projector. Then, among all p -dimensional $V \subset \text{Null}(\mathbf{H})$, provided $\mu_{p+1} > 0$,

$$\begin{aligned} \min_{\dim(V)=p} \sup_{\mathbf{x}_n \in \mathcal{M}_\tau} \|(\mathbf{I} - P_V)\mathbf{x}_n\|_2^2 &= \\ \sup_{\mathbf{x}_n \in \mathcal{M}_\tau} \|(\mathbf{I} - P_{V_p})\mathbf{x}_n\|_2^2 &= \frac{\tau}{\mu_{p+1}}. \end{aligned}$$

Proof.

Expand any $\mathbf{x}_n \in \text{Null}(\mathbf{H})$ in the eigenbasis of \mathbf{T} : $\mathbf{x}_n = \sum_{j=1}^q a_j \mathbf{v}_j$ with $\|\mathbf{x}_n\|_2^2 = \sum_j a_j^2$ and energy constraint $\mathbf{x}_n^\top \mathbf{T} \mathbf{x}_n = \sum_j \mu_j a_j^2 \leq \tau$. This is the Rayleigh–Ritz parameterization for a symmetric PSD matrix. Take $V_p = \text{span}\{\mathbf{v}_1, \dots, \mathbf{v}_p\}$. Then $(\mathbf{I} - P_{V_p})\mathbf{x}_n = \sum_{j \geq p+1} a_j \mathbf{v}_j$, hence

$$\|(\mathbf{I} - P_{V_p})\mathbf{x}_n\|_2^2 = \sum_{j \geq p+1} a_j^2 \leq \frac{1}{\mu_{p+1}} \sum_{j \geq p+1} \mu_j a_j^2 \leq \frac{\tau}{\mu_{p+1}}.$$

The first inequality uses $\mu_j \geq \mu_{p+1}$ for all $j \geq p+1$. Equality is attained by $\mathbf{x}_n^* = \sqrt{\tau/\mu_{p+1}} \mathbf{v}_{p+1}$, so

$$\sup_{\mathbf{x}_n \in \mathcal{M}_\tau} \|(\mathbf{I} - P_{V_p})\mathbf{x}_n\|_2^2 = \frac{\tau}{\mu_{p+1}}. \quad (*)$$

Let V be any p -dimensional subspace of $\text{Null}(\mathbf{H})$ and set $W := V^\perp$ (within $\text{Null}(\mathbf{H})$), so $\dim W = q - p$. Consider the restricted eigenproblem for \mathbf{T} on W ; denote its smallest eigenvalue by

$$\tilde{\mu}_{\min}(W) = \min_{\mathbf{u} \in W, \|\mathbf{u}\|=1} \mathbf{u}^\top \mathbf{T} \mathbf{u}.$$

By the Courant–Fischer min–max theorem,

$$\begin{aligned} \mu_{p+1} &= \max_{\dim(S)=q-p} \min_{\mathbf{u} \in S, \|\mathbf{u}\|=1} \mathbf{u}^\top \mathbf{T} \mathbf{u} \\ &\geq \min_{\mathbf{u} \in W, \|\mathbf{u}\|=1} \mathbf{u}^\top \mathbf{T} \mathbf{u} = \tilde{\mu}_{\min}(W). \end{aligned} \quad (20)$$

Thus $\tilde{\mu}_{\min}(W) \leq \mu_{p+1}$.

Now maximize the residual under the energy constraint within W , where the projection vanishes: for any $\mathbf{x}_n \in W$, $(\mathbf{I} - P_V)\mathbf{x}_n = \mathbf{x}_n$. The maximizer aligns with the eigenvector of $\mathbf{T}|_W$ for $\tilde{\mu}_{\min}(W)$, yielding

$$\begin{aligned} \sup_{\mathbf{x}_n \in \mathcal{M}_\tau} \|(\mathbf{I} - P_V)\mathbf{x}_n\|_2^2 &\geq \sup_{\substack{\mathbf{x}_n \in W \\ \mathbf{x}_n^\top \mathbf{T} \mathbf{x}_n \leq \tau}} \|\mathbf{x}_n\|_2^2 = \frac{\tau}{\tilde{\mu}_{\min}(W)} \\ &\geq \frac{\tau}{\mu_{p+1}}. \end{aligned} \quad (\dagger)$$

Combining $(*)$ and (\dagger) gives

$$\min_{\dim(V)=p} \sup_{\mathbf{x}_n \in \mathcal{M}_\tau} \|(\mathbf{I} - P_V)\mathbf{x}_n\|_2^2 = \frac{\tau}{\mu_{p+1}},$$

with the minimum attained at $V = V_p$.

Remark 3 The constraint $\mathbf{x}_n^\top \mathbf{T} \mathbf{x}_n \leq \tau$ is an ellipsoid aligned with the eigenvectors of \mathbf{T} . The largest Euclidean norm inside this ellipsoid occurs along the smallest eigenvalue direction. If the subspace V leaves a small- μ direction outside, an adversary can place all energy there and produce a large residual. Courant–Fischer formalizes this: every p -dimensional V leaves some direction with Rayleigh quotient $\leq \mu_{p+1}$ in V^\perp .

Selecting $V_p = \text{span}\{\mathbf{v}_1, \dots, \mathbf{v}_p\}$ “covers” all directions with the smallest graph energy (smoothest modes). The worst direction you do not cover is then \mathbf{v}_{p+1} with energy μ_{p+1} , making the worst-case miss exactly τ/μ_{p+1} . Any other choice leaves an even smoother (smaller μ) direction uncovered, increasing the worst-case error.

The bound quantifies how quickly the worst-case miss decays as p grows: the key driver is μ_{p+1} . For graph Laplacians, $\{\mu_j\}$ increases smoothly, so μ_{p+1} grows and the miss shrinks rapidly; for $\mathbf{L} = \mathbf{I}$, $\mathbf{T} = \mathbf{P}_n$ has a flat spectrum on $\text{Null}(\mathbf{H})$, so μ_{p+1} is constant and the bound does not improve. This explains why graph-limited designs achieve much better null-space coverage than geometry-free design choices (the argument is the Kolmogorov n -width of the ellipsoid $\{\mathbf{x}_n : \mathbf{x}_n^\top \mathbf{T} \mathbf{x}_n \leq \tau\}$).

A3. Proof of Proposition 1

Proposition 1 (Per-mode predictability bound) Let $\mathbf{x} \in \mathbb{R}^n$ be zero-mean Gaussian with covariance \mathbf{C} and precision $\mathbf{Q} = \mathbf{C}^{-1}$. Let $\mathbf{H} \in \mathbb{R}^{m \times n}$ and denote the orthogonal projectors onto $\mathcal{R} := \text{Range}(\mathbf{H}^\top)$ and $\mathcal{N} := \text{Null}(\mathbf{H})$ by \mathbf{P}_r and \mathbf{P}_n , respectively. Block \mathbf{Q} and \mathbf{C} with respect to the decomposition $\mathbb{R}^n = \mathcal{R} \oplus \mathcal{N}$:

$$\mathbf{Q} = \begin{bmatrix} \mathbf{Q}_{rr} & \mathbf{Q}_{rn} \\ \mathbf{Q}_{nr} & \mathbf{Q}_{nn} \end{bmatrix}, \quad \mathbf{C} = \begin{bmatrix} \mathbf{C}_{rr} & \mathbf{C}_{rn} \\ \mathbf{C}_{nr} & \mathbf{C}_{nn} \end{bmatrix}.$$

Assume $\mathbf{Q}_{nn} \succ 0$ on \mathcal{N} and let $\{\mathbf{v}_j\}$ be an orthonormal eigenbasis of \mathbf{Q}_{nn} with $\mathbf{Q}_{nn} \mathbf{v}_j = \mu_j \mathbf{v}_j$ and $\mu_j > 0$. Define the j -th null coefficient $a_j := \mathbf{v}_j^\top \mathbf{x}_n$ where $\mathbf{x}_n := \mathbf{P}_n \mathbf{x}$. Consider measurements from (1) and denote $\mathbf{C}_y := \mathbf{H} \mathbf{C}_{rr} \mathbf{H}^\top + \sigma^2 \mathbf{I}_m$. Then the population R^2 of the optimal linear predictor of a_j from \mathbf{y} satisfies

$$\rho_j^2 := \frac{\text{Cov}(a_j, \mathbf{y})^\top \mathbf{C}_y^{-1} \text{Cov}(\mathbf{y}, a_j)}{\text{Var}(a_j)} \leq \frac{c_j}{c_j + \mu_j},$$

$$c_j := \mathbf{v}_j^\top (\mathbf{Q}_{rn} \mathbf{C}_{rr} \mathbf{Q}_{nr}) \mathbf{v}_j.$$

Equality holds in the ideal case $\mathbf{H} = \mathbf{I}$ and $\sigma^2 = 0$.

Since $\mathbf{Q} \succ 0$ and $\mathbf{Q}_{nn} \succ 0$, the block inverse of \mathbf{Q} exists and yields the standard formulas (Schur complements)

$$\begin{aligned} \mathbf{C}_{nr} &= -\mathbf{Q}_{nn}^{-1}\mathbf{Q}_{nr}\mathbf{C}_{rr}, \\ \mathbf{C}_{nn} &= \mathbf{Q}_{nn}^{-1} + \mathbf{Q}_{nn}^{-1}\mathbf{Q}_{nr}\mathbf{C}_{rr}\mathbf{Q}_{rn}\mathbf{Q}_{nn}^{-1}. \end{aligned} \quad (21)$$

They follow from

$$\mathbf{Q}^{-1} = \begin{bmatrix} \cdot & \cdot & \cdot & \cdot & \cdot & \cdot \\ \cdot & \cdot & \cdot & \cdot & \cdot & \cdot \\ \cdot & \cdot & \cdot & \cdot & \cdot & \cdot \\ \cdot & \cdot & \cdot & \cdot & \cdot & \cdot \\ \cdot & \cdot & \cdot & \cdot & \cdot & \cdot \\ \cdot & \cdot & \cdot & \cdot & \cdot & \cdot \end{bmatrix}$$

By definition $a_j = \mathbf{v}_j^\top \mathbf{x}_n$ and $\mathbf{y} = \mathbf{H}\mathbf{x}_r + \boldsymbol{\omega}$ with $\boldsymbol{\omega} \perp \mathbf{x}$. Hence

$$\text{Cov}(a_j, \mathbf{y}) = \mathbf{v}_j^\top \text{Cov}(\mathbf{x}_n, \mathbf{H}\mathbf{x}_r) = \mathbf{v}_j^\top \mathbf{C}_{nr}\mathbf{H}^\top. \quad (22)$$

Using (21), this becomes

$$\text{Cov}(a_j, \mathbf{y}) = -\mathbf{v}_j^\top \mathbf{Q}_{nn}^{-1}\mathbf{Q}_{nr}\mathbf{C}_{rr}\mathbf{H}^\top.$$

Therefore the *numerator* of ρ_j^2 is

$$\begin{aligned} \text{Num} &= \text{Cov}(a_j, \mathbf{y})^\top \mathbf{C}_y^{-1} \text{Cov}(a_j, \mathbf{y}) \\ &= \mathbf{H}\mathbf{C}_{rr}\mathbf{Q}_{rn}\mathbf{Q}_{nn}^{-1}\mathbf{v}_j \cdot \mathbf{C}_y^{-1} \cdot \mathbf{v}_j^\top \mathbf{Q}_{nn}^{-1}\mathbf{Q}_{nr}\mathbf{C}_{rr}\mathbf{H}^\top. \end{aligned} \quad (23)$$

Introduce $\mathbf{A} := \mathbf{H}\mathbf{C}_{rr}^{1/2}$ and note $\mathbf{C}_y = \mathbf{A}\mathbf{A}^\top + \sigma^2\mathbf{I}$. Define also

$$\mathbf{M} := \mathbf{C}_{rr}^{1/2}\mathbf{H}^\top \mathbf{C}_y^{-1} \mathbf{H}\mathbf{C}_{rr}^{1/2} = \mathbf{A}^\top (\mathbf{A}\mathbf{A}^\top + \sigma^2\mathbf{I})^{-1} \mathbf{A}.$$

Let $\mathbf{w}_j := \mathbf{C}_{rr}^{1/2}\mathbf{Q}_{rn}\mathbf{Q}_{nn}^{-1}\mathbf{v}_j$. Then (23) rewrites compactly as

$$\text{Num} = \mathbf{w}_j^\top \mathbf{M} \mathbf{w}_j. \quad (24)$$

Take an SVD $\mathbf{A} = \mathbf{V}\mathbf{S}\mathbf{V}^\top$, $\mathbf{S} = \text{diag}(s_i) \geq 0$. Then

$$\mathbf{M} = \mathbf{V}\mathbf{S}(\mathbf{S}^2 + \sigma^2\mathbf{I})^{-1}\mathbf{S}\mathbf{V}^\top = \mathbf{V} \text{diag}\left(\frac{s_i^2}{s_i^2 + \sigma^2}\right)\mathbf{V}^\top \preceq \mathbf{I},$$

with equality iff $\sigma^2 = 0$ (and then $\mathbf{M} = \mathbf{I}$). Consequently,

$$\text{Num} = \mathbf{w}_j^\top \mathbf{M} \mathbf{w}_j \leq \mathbf{w}_j^\top \mathbf{w}_j = \mathbf{v}_j^\top \mathbf{Q}_{nn}^{-1}\mathbf{Q}_{nr}\mathbf{C}_{rr}\mathbf{Q}_{rn}\mathbf{Q}_{nn}^{-1}\mathbf{v}_j. \quad (25)$$

Using (21),

$$\begin{aligned} \text{Den} &:= \text{Var}(a_j) = \mathbf{v}_j^\top \mathbf{C}_{nn}\mathbf{v}_j \\ &= \mathbf{v}_j^\top \mathbf{Q}_{nn}^{-1}\mathbf{v}_j + \mathbf{v}_j^\top \mathbf{Q}_{nn}^{-1}\mathbf{Q}_{nr}\mathbf{C}_{rr}\mathbf{Q}_{rn}\mathbf{Q}_{nn}^{-1}\mathbf{v}_j. \end{aligned} \quad (26)$$

Since $\mathbf{Q}_{nn}\mathbf{v}_j = \mu_j\mathbf{v}_j$ and $\|\mathbf{v}_j\|_2 = 1$, we have

$$\mathbf{Q}_{nn}^{-1}\mathbf{v}_j = \mu_j^{-1}\mathbf{v}_j, \quad \mathbf{v}_j^\top \mathbf{Q}_{nn}^{-1}\mathbf{v}_j = \mu_j^{-1}.$$

Define the scalar

$$c_j := \mathbf{v}_j^\top (\mathbf{Q}_{rn}\mathbf{C}_{rr}\mathbf{Q}_{nr})\mathbf{v}_j \geq 0,$$

and observe that

$$\mathbf{v}_j^\top \mathbf{Q}_{nn}^{-1}\mathbf{Q}_{nr}\mathbf{C}_{rr}\mathbf{Q}_{rn}\mathbf{Q}_{nn}^{-1}\mathbf{v}_j = \mu_j^{-2} c_j.$$

Plugging into (26) gives

$$\text{Den} = \mu_j^{-1} + \mu_j^{-2} c_j. \quad (27)$$

From (25) and (27),

$$\rho_j^2 = \frac{\text{Num}}{\text{Den}} \leq \frac{\mu_j^{-2} c_j}{\mu_j^{-1} + \mu_j^{-2} c_j} = \frac{c_j}{c_j + \mu_j}.$$

If $\sigma^2 = 0$ and $\mathbf{H} = \mathbf{I}$, then $\mathbf{C}_y = \mathbf{C}_{rr}$ and hence $\mathbf{M} = \mathbf{I}$, so inequality (25) is an equality and $\rho_j^2 = \frac{c_j}{c_j + \mu_j}$.

A4. Graph structures

A4.1. Additional graphs

We analyze two additional graph topologies.

Random-walk normalized graph (\mathbf{L}_{rw}). Starting from an undirected graph with adjacency \mathbf{A} and degree matrix \mathbf{D} , The random-walk normalized Laplacian is

$$\mathbf{L}_{\text{rw}} = \mathbf{I} - \mathbf{D}^{-1}\mathbf{A}.$$

It can be read as $\mathbf{L}_{\text{rw}} = \mathbf{I} - \mathbf{P}$, where $\mathbf{P} = \mathbf{D}^{-1}\mathbf{A}$ is the one-step Markov transition; hence $\mathbf{L}_{\text{rw}}\mathbf{1} = \mathbf{0}$ and the spectrum reflects how probability mass mixes locally. This normalization corrects for degree imbalance: edges from low-degree nodes are not underweighted, so the quadratic form $\mathbf{x}^\top \mathbf{L}_{\text{rw}}\mathbf{x}$ penalizes variations relative to local node degree. In our pipeline, we never use \mathbf{L}_{rw} directly; we act on the null component through the null-restricted operator $\mathbf{T} = \mathbf{P}_n \mathbf{L}_{\text{rw}} \mathbf{P}_n$ and compute its smooth eigenmodes to build \mathbf{S} .

Symmetric normalized graph (\mathbf{L}_{sym}). The symmetric normalized Laplacian is

$$\mathbf{L}_{\text{sym}} = \mathbf{I} - \mathbf{D}^{-1/2}\mathbf{A}\mathbf{D}^{-1/2},$$

which is symmetric positive semidefinite and yields the energy $\mathbf{x}^\top \mathbf{L}_{\text{sym}}\mathbf{x} = \frac{1}{2} \sum_{i,j} w_{ij} \left(\frac{x_i}{\sqrt{d_i}} - \frac{x_j}{\sqrt{d_j}} \right)^2$. It equalizes contributions across nodes with different degrees and, on regular grids, is similar to \mathbf{L}_{rw} (hence they share eigenvalues up to a similarity transform). Within GSNR, we apply the same null restriction $\mathbf{T} = \mathbf{P}_n \mathbf{L}_{\text{sym}} \mathbf{P}_n$ and take its p smallest eigenpairs to span the graph-smooth null subspace used by \mathbf{S} . In practice, both normalizations deliver the intended effect, concentrating smooth, predictable variation in $\text{Null}(\mathbf{H})$, with small empirical differences that reflect how degree reweighting shapes the spectrum of \mathbf{T} .

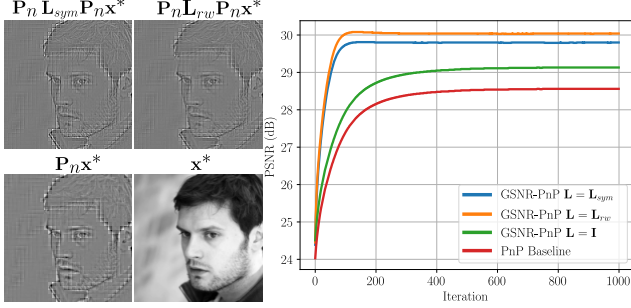


Figure 8. SR with different graph Laplacians. Left: ground truth x^* , its null component $P_n x^*$, and graph-smoothed null responses $P_n L_{\text{sym}} P_n x^*$ and $P_n L_{\text{rw}} P_n x^*$. Right: PSNR vs. iteration for GSNR-PnP with $L \in \{L_{\text{sym}}, L_{\text{rw}}, I\}$, and the PnP baseline.

In Figure 8, the left panels visualize the invisible component and its graph-smoothed variants: $P_n x^*$ (bottom-left) highlights edges and fine textures that lie in the null space of the sensing operator, while applying the null-restricted Laplacians $P_n L_{\text{sym}} P_n$ and $P_n L_{\text{rw}} P_n$ further emphasizes coherent edge geometry and suppresses isolated, high-frequency speckles. The two normalizations yield very similar structures, with L_{rw} marginally enhancing sharp contours, consistent with its degree-normalized reweighting. This visual evidence aligns with the goal of GSNR: to impose structure *only* in the null space and make its content smoother and more predictable.

The PSNR-iteration curves (right) show that graph-limited null-space designs (GSNR-PnP with L_{sym} or L_{rw}) both *converge faster* and *stabilize at higher PSNR* than the geometry-free alternative ($L = I$) and the PnP baseline. Among the graph choices, the L_{rw} variant exhibits the steepest initial rise and the highest plateau, while L_{sym} tracks closely behind; both consistently dominate $L = I$. This behavior matches the theory: normalized Laplacians produce a more informative spectrum for the null-restricted operator $T = P_n L P_n$, yielding higher spectral coverage and stronger statistical coupling, which in turn improves both the fixed point (final PSNR) and the transient (speed of convergence).

A4.2. Learning a Structured Laplacian

The learning objective maximizes the average coverage over a prescribed set \mathcal{P} (typically 10 equispaced values):

$$\max_{L_\theta \succeq 0} \frac{1}{|\mathcal{P}|} \sum_{p \in \mathcal{P}} C(p),$$

using $T = P_n L_\theta P_n$ for the creation of S as in Sec. 3.2. Each parametrization enforces $L_\theta \succeq 0$ via a symmetric construction plus a small εI to keep eigenvalues nonnegative.

Dense (low-rank PSD). Learn $\Theta \in \mathbb{R}^{n \times r}$:

$$L_\theta = \Theta \Theta^\top + \varepsilon I.$$

Diagonal. Let $\theta \in \mathbb{R}^n$ be learnable logits and define $\text{softplus}(t) \triangleq \log(1 + e^t)$. Set

$$d = \text{softplus}(\theta) + \varepsilon, \quad L_\theta = \text{diag}(d).$$

Circulant (wrap-around convolution). Learn a kernel $\Theta \in \mathbb{R}^{E \times E}$; let $C_{\text{circ}}(\Theta) \in \mathbb{R}^{n \times n}$ denote the circular (wrap-around) convolution operator on vectorized images. Then

$$L_\theta = C_{\text{circ}}(\Theta)^\top C_{\text{circ}}(\Theta) + \varepsilon I.$$

Block-diagonal. Partition n into $b = n/B$ blocks of size B . Learn $\Theta_i \in \mathbb{R}^{B \times B}$ for $i = 1, \dots, b$. With

$$\text{blockdiag}(\mathbf{A}_1, \dots, \mathbf{A}_b) \triangleq \begin{bmatrix} \mathbf{A}_1 & & \\ & \ddots & \\ & & \mathbf{A}_b \end{bmatrix},$$

we set

$$L_\theta = \text{blockdiag}(\Theta_1 \Theta_1^\top + \varepsilon I_B, \dots, \Theta_b \Theta_b^\top + \varepsilon I_B).$$

Fig. 9 shows the comparison of a) normalized T -eigenvalues and b) S -coverage for the different parametrizations of L_θ . Using a Laplacian graph such as L_{8nn} in GSNR yields the best spectral performance and coverage for any value of p . Although NPN has an adequate spectrum, its coverage is very limited, whereas the opposite is true for block-diag.

A5. Settings for construction null-restricted Laplacian in practice

We never materialize P_n or T as dense matrices. Instead, $P_n v = v - H^\top (H H^\top)^{-1} H v$ is exposed as a callable projector using a factorization of $H H^\top$, and T is wrapped as a SciPy `LinearOperator` that applies $T x = P_n (L P_n x)$ on the fly. We then invoke ARPACK [24] via `eigsh` with spectral method to extract the k smallest-magnitude eigenpairs of T (the smoothest graph-null modes), respecting the constraint $k \leq n$ and defaulting to $k = \min(q, n - 1)$ when unspecified. The routine returns eigenvectors as columns $U \in \mathbb{R}^{n \times k}$ and eigenvalues $\{\mu_j\}$; we set $S_{\text{full}} = U^\top$ so that the rows of S form an orthonormal basis of the selected null-space subspace, and finally truncate to the first p rows for training/inference. The process is performed for different graph Laplacians L , and the structure selection is guided by our spectral criteria, i.e., maximum coverage/predictability over the first p modes. The *demosaiicing* case follows the same flow but loads a precomputed sparse H , optionally

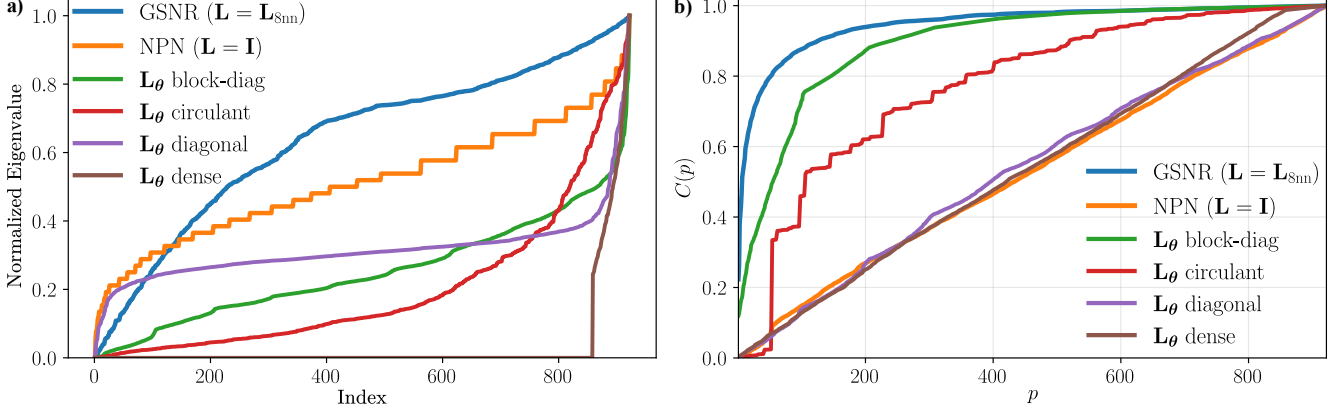


Figure 9. (a) Variation of \mathbf{T} normalized eigenvalues for \mathbf{L}_θ with respect to their index in CS. (b) Coverage of \mathbf{S} with \mathbf{L}_θ in CS.

lifts the Laplacian to multi-channel form with a Kronecker product $\mathbf{L} \leftarrow \mathbf{I}_C \otimes \mathbf{L}$.

For the numerical results of this work, we empirically set the dimension p . However, our framework provides a principled evaluation on how to select p based on the null-space coverage. Let $\lambda = (\lambda_1, \dots, \lambda_q)$ be the eigenvalues of $\text{Cov}(\mathbf{x}_n)$ in the graph-smooth basis, ordered so that $\lambda_1 \geq \dots \geq \lambda_q > 0$. Define the cumulative coverage $C(p) = (\sum_{i=1}^p \lambda_i) / (\sum_{i=1}^q \lambda_i)$. We select the effective dimension p^* as the smallest p that simultaneously achieves a target coverage level and lies on a plateau of the coverage curve, following Algorithm 1.

Algorithm 1 Coverage-based automatic selection of p

Require: Eigenvalues $\lambda_1 \geq \dots \geq \lambda_q > 0$; coverage target $\kappa \in (0, 1)$ (e.g. $\kappa = 0.95$); slope tolerance $\delta > 0$ (e.g. $\delta = 10^{-3}$); plateau length $L \in \mathbb{N}$ (e.g. $L = 10$).

- 1: Compute total variance $S \leftarrow \sum_{i=1}^q \lambda_i$.
- 2: For $p = 1, \dots, q$, compute coverage $C(p) \leftarrow (\sum_{i=1}^p \lambda_i) / S$.
- 3: For $p = 1, \dots, q$, compute incremental gains $\Delta C(p) \leftarrow C(p) - C(p-1)$, with $C(0) \equiv 0$.
- 4: **for** $p = 1, \dots, q$ **do**
- 5: **if** $C(p) \geq \kappa$ **then**
- 6: Check plateau condition:
 $\max\{\Delta C(p), \dots, \Delta C(\min(p+L-1, q))\} \leq \delta$.
- 7: **if** plateau condition holds **then**
- 8: **return** $p^* \leftarrow p$.
- 9: **end if**
- 10: **end if**
- 11: **end for**
- 12: If no p satisfies the above, set $p^* \leftarrow q$ (use all modes).

A6. Ablation Studies of the Graph Regularizer

Recall that GSNR is *solver-agnostic*: it augments the data-fidelity objective with the terms $\gamma \|G^*(\mathbf{y}) - \mathbf{S}\mathbf{x}\|_2^2 + \frac{\gamma_g}{2} \mathbf{x}^\top \mathbf{T}\mathbf{x}$. Consequently, GSNR can be incorporated into

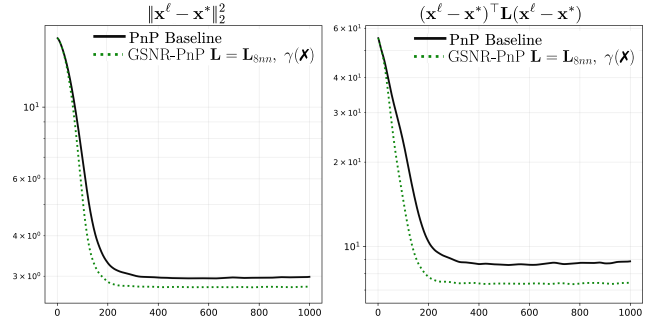


Figure 10. PnP variant with null-only projector regularizer: illustrative convergence.

any iterative solver, e.g., ADMM, HQS, FISTA, PD, or diffusion-based methods (see A8), by including these terms in its \mathbf{x} -update. Before showing further experiments, we describe the baseline algorithms and the GSNR versions.

Plug-and-Play. In this case, we used the PGD-PnP method. Algorithm 2 shows the GSNR PnP-PGD modification.

Algorithm 2 GSNR PnP-PGD with null-space and graph regularization

Require: $K, \mathbf{H}, \mathbf{y}, \alpha, \omega, \gamma, \gamma_g, G^*, \mathbf{S}$

1: $\mathbf{x}_0 = \mathbf{H}^\top \mathbf{y} + \mathbf{S}^\top G^*(\mathbf{y})$

2: **for** $i = 1, \dots, K$ **do**

3:

$$\mathbf{x}_i \leftarrow \mathbf{x}_{i-1} - \alpha \left(\mathbf{H}^\top (\mathbf{H}\mathbf{x}_{i-1} - \mathbf{y}) + \gamma \mathbf{S}^\top (\mathbf{S}\mathbf{x}_{i-1} - G^*(\mathbf{y})) + \gamma_g \mathbf{T}\mathbf{x}_{i-1} \right)$$

4: $\mathbf{x}_i \leftarrow D_\omega(\mathbf{x}_i)$

5: **end for**

6: **return** \mathbf{x}_i

A6.1. Why graph smooth null-space?

An initial test that shows us the usefulness of the null-space Laplacian is to start from the assumption that the reconstruction error with respect to the ground-truth, $\mathbf{x}_n^\ell = \mathbf{x}^\ell - \mathbf{x}^*$ is the null-space. Fig. 10 shows the convergence of the

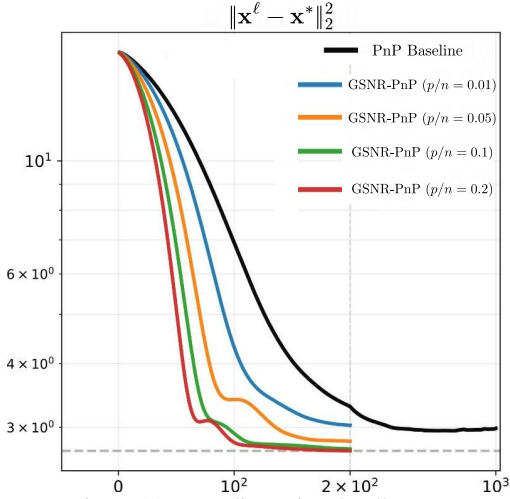


Figure 11. Low-dimensional null-space.

reconstruction and how the null-laplacian regularizer behaves. The baseline (black) shows that improving the quality of our reconstruction also reduces the null-laplacian error $(\mathbf{x}_n^\ell)^\top \mathbf{L}(\mathbf{x}_n^\ell)$, even though this term is not considered in the PnP cost function. Adding this term (green) would further improve the reconstruction. This demonstrates the usefulness of including a regularizer that promotes a graph-limited null-space.

A6.2. Why low-dimensional null-space projections?

Fig. 11 shows the convergence of the reconstruction when using different values of p . It can be seen that as the value of p increases, the reconstruction error decreases; however, this reaches a limit, since from $p/n = 0.1$ onward, the gain decreases. These results justify the need to use low-dimensional null-space projections, as they enable higher-quality reconstruction without being significantly affected by the decrease in predictability.

A6.3. Cost-function ablation

Figure 12 highlights two effects of the GSNR design: improved conditioning through the null-only graph regularizer and sensitivity to the choice of Laplacian in demosaicing problem. All GSNR-PnP variants eventually reach a similar high PSNR plateau, slightly above the PnP baseline, showing that incorporating the graph-smooth null-space prior does not harm the final reconstruction quality and can modestly improve it. However, the convergence speed differs significantly: when γ_g is active, GSNR-PnP with \mathbf{L}_{4nn} or \mathbf{L}_{8nn} reaches its peak PSNR in far fewer iterations than both the geometry-free $\mathbf{L} = \mathbf{I}$ case and the baseline.

When the graph regularizer is turned off, the graph-based methods still outperform the baseline but converge more slowly, with trajectories that are closer to the standard PnP. This confirms the theoretical prediction that the null-only graph term improves the spectrum of the normal matrix, ef-

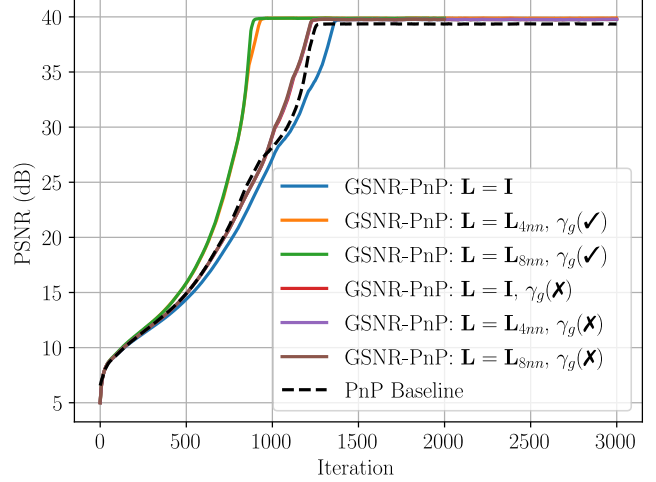


Figure 12. Effect of the null-only graph regularizer on GSNR-PnP convergence for demosaicing. We plot PSNR versus iteration for GSNR-PnP with different Laplacians ($\mathbf{L} = \mathbf{I}, \mathbf{L}_{4nn}, \mathbf{L}_{8nn}$) and with the graph-regularization weight γ_g either enabled or disabled, along with the standard PnP baseline (dashed).

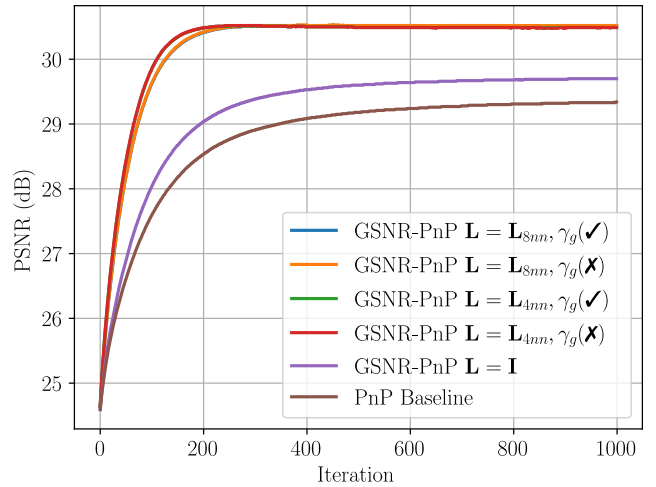


Figure 13. Effect of the null-only graph regularizer on GSNR-PnP convergence for super-resolution. We plot PSNR versus iteration for GSNR-PnP with different Laplacians ($\mathbf{L} = \mathbf{I}, \mathbf{L}_{4nn}, \mathbf{L}_{8nn}$) and with the graph-regularization weight γ_g either enabled or disabled, along with the standard PnP baseline (dashed).

fectively “lifting” the null directions, while the GSNR basis itself governs the final achievable PSNR. In practice, combining a graph Laplacian with a nonzero γ_g yields the best trade-off: fast convergence to high-quality solutions with minimal overhead in the PnP update. Similar analysis and results are shown in Fig. 13, for the image super-resolution problem, where the graph regularizer slightly increases convergence speed.

A6.4. Minimax optimality bound

To experimentally validate the theory of Theorem 2, two different operators \mathbf{S} were tested with $p = 0.1n$ and $\tau = 1$

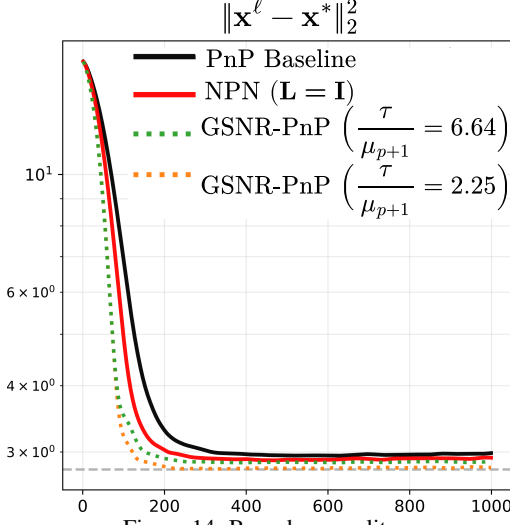


Figure 14. Bound vs. quality.

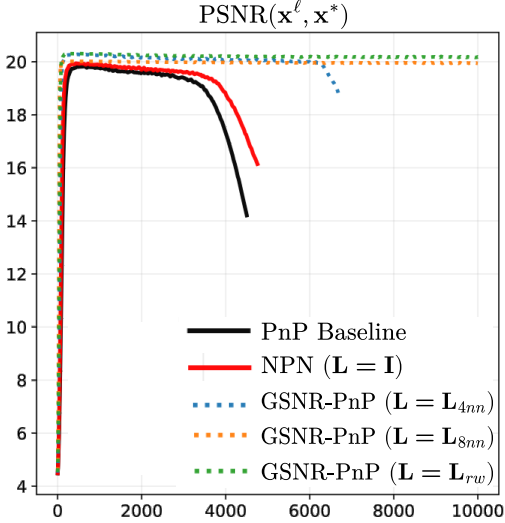


Figure 15. Fixed-point convergence.

for Fig. 14. In the green and yellow cases, there are two extreme values of the bound $\frac{\tau}{\mu_{p+1}}$ that demonstrate the theorem’s postulate, since a \mathbf{S} with a lower bound (2.25) results in better reconstruction.

A6.5. Fixed-point convergence

When analyzing an extreme case in Fig. 15, it can be observed that the proposed GSNR method (dotted lines) converges to a fixed point without diverging as iterations progress, achieving even faster convergence than NPN and the baseline.

A7. Coverage curve

Figure 16 shows that graph-based Laplacians concentrate null-space variance into a small number of modes. For \mathbf{L}_{4nn} , \mathbf{L}_{rw} , and \mathbf{L}_{sym} , the coverage rises steeply and reaches

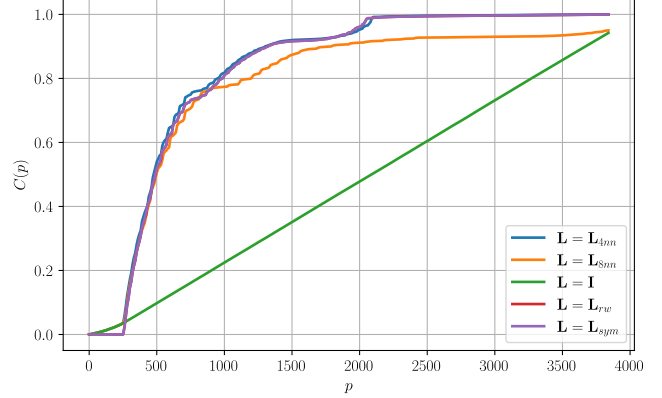


Figure 16. Spectral coverage curves $C(p)$ for super-resolution, comparing different Laplacian choices in the GSNR construction: grid \mathbf{L}_{4nn} , grid \mathbf{L}_{8nn} , random-walk normalized \mathbf{L}_{rw} , symmetric normalized \mathbf{L}_{sym} , and the geometry-free baseline $\mathbf{L} = \mathbf{I}$. Coverage $C(p)$ is the fraction of null-space variance captured by the first p graph-smooth modes.

almost full variance with only a fraction of the null-space dimension, whereas the identity Laplacian $\mathbf{L} = \mathbf{I}$ exhibits an almost perfectly linear curve $C(p) \approx p/q$, meaning that coverage grows only proportionally to the dimension, and no “early” compression occurs. The \mathbf{L}_{8nn} graph still offers a substantial advantage over $\mathbf{L} = \mathbf{I}$. But its curve saturates below the others, indicating slightly less concentrated variance. Overall, These results confirm the theoretical prediction that graph-smooth null modes provide much better coverage than geometry-free bases: a relatively small p already captures most null-space energy for the normalized and grid Laplacians, while the identity requires many more modes to achieve

A8. GSNR inclusion in Diffusion-based solvers

A8.1. DPS [8].

We denote N is the number of reverse diffusion steps, and $i \in \{0, \dots, N - 1\}$ is the reverse-time index; $\mathbf{x}_i \in \mathbb{R}^n$ is the current latent state and $\mathbf{x}_N \sim \mathcal{N}(\mathbf{0}, \mathbf{I})$ is the Gaussian start; $\hat{\mathbf{s}} = \mathbf{s}_\theta(\mathbf{x}_i, i)$ is the score/noise estimate produced by the network with parameters θ ; $\hat{\mathbf{x}}_0$ is the network’s prediction of the clean sample at step i ; $\alpha_i \in (0, 1]$ is the per-step retention factor, $\beta_i = 1 - \alpha_i$ is the noise increment, and $\bar{\alpha}_i = \prod_{j=1}^i \alpha_j$ is the cumulative product (with $\bar{\alpha}_0 = 1$); $\zeta_i > 0$ is the data-consistency step size and $\tilde{\sigma}_i \geq 0$ is the sampling noise scale at step i ; $\mathbf{z} \sim \mathcal{N}(\mathbf{0}, \mathbf{I})$ is i.i.d. Gaussian noise; \mathbf{x}'_{i-1} denotes the pre-data-consistency iterate before applying the gradient correction. In the GSNR version, we further introduce a learned null-space predictor $\mathbf{G}(\mathbf{y}) \approx \mathbf{S}\mathbf{x}^*$ and a weight $\gamma > 0$ for the graph-smooth null-space penalty $\|\mathbf{G}(\mathbf{y}) - \hat{\mathbf{S}}\mathbf{x}_0\|_2^2$. Algorithm 3 shows the integration of GSNR in DPS.

Algorithm 3 GSNR–DPS Sampling with null-space and graph regularization

Require: $K, \mathbf{H}, \mathbf{y}, \{\zeta_i\}_{i=1}^K, \{\tilde{\sigma}_i\}_{i=1}^K, \gamma, \gamma_g, \mathbf{S}, \mathbf{G}^*, \mathbf{P}_n, \mathbf{L}$

- 1: $\mathbf{x}_K \sim \mathcal{N}(\mathbf{0}, \mathbf{I})$
- 2: **for** $i = K-1, \dots, 0$ **do**
- 3: $\hat{\mathbf{s}} \leftarrow \mathbf{s}_\theta(\mathbf{x}_i, i)$
- 4: $\hat{\mathbf{x}}_0 \leftarrow \frac{1}{\sqrt{\alpha_i}}(\mathbf{x}_i + (1 - \alpha_i)\hat{\mathbf{s}})$
- 5: $\mathbf{z} \sim \mathcal{N}(\mathbf{0}, \mathbf{I})$
- 6: $\mathbf{x}'_{i-1} \leftarrow \frac{\sqrt{\alpha_i(1-\alpha_{i-1})}}{1-\alpha_i} \mathbf{x}_i + \frac{\sqrt{\alpha_{i-1}\beta_i}}{1-\alpha_i} \hat{\mathbf{x}}_0 + \tilde{\sigma}_i \mathbf{z}$
- 7: $\mathbf{x}_{i-1} \leftarrow \mathbf{x}'_{i-1} - \zeta_i \nabla_{\mathbf{x}_i} \left[\|\mathbf{y} - \mathbf{H}\hat{\mathbf{x}}_0\|_2^2 + \gamma \|\mathbf{G}^*(\mathbf{y}) - \mathbf{S}\hat{\mathbf{x}}_0\|_2^2 + \gamma_g \|\mathbf{P}_n \mathbf{L} \hat{\mathbf{x}}_0\|_2^2 \right]$
- 8: **end for**
- 9: **return** $\hat{\mathbf{x}}_0$

Algorithm 4 GSNR–DiffPIR Sampling null-space and graph regularization

Require: $K, \mathbf{H}, \mathbf{y}, \sigma_n, \{\tilde{\sigma}_i\}_{i=1}^K, \zeta, \omega, \gamma, \gamma_g, \mathbf{S}, \mathbf{G}^*, \mathbf{P}_n, \mathbf{L}$

- 1: Precompute $\rho_i \leftarrow \omega \sigma_n^2 / \tilde{\sigma}_i^2$ for $i = 1, \dots, K$
- 2: $\mathbf{x}_K \sim \mathcal{N}(\mathbf{0}, \mathbf{I})$
- 3: **for** $i = K, \dots, 1$ **do**
- 4: $\hat{\mathbf{s}} \leftarrow \mathbf{s}_\theta(\mathbf{x}_i, i)$
- 5: $\hat{\mathbf{x}}_0^{(i)} \leftarrow \frac{1}{\sqrt{\alpha_i}}(\mathbf{x}_i + (1 - \alpha_i)\hat{\mathbf{s}})$
- 6: $\hat{\mathbf{x}}_0^{(i)} \leftarrow \arg \min_{\mathbf{x}} \|\mathbf{y} - \mathbf{H}\mathbf{x}\|_2^2 + \rho_i \|\mathbf{x} - \hat{\mathbf{x}}_0^{(i)}\|_2^2 + \gamma \|\mathbf{G}^*(\mathbf{y}) - \mathbf{S}\mathbf{x}\|_2^2 + \gamma_g \|\mathbf{P}_n \mathbf{L} \mathbf{x}\|_2^2$
- 7: $\hat{\mathbf{e}} \leftarrow \frac{1}{\sqrt{1-\alpha_i}}(\mathbf{x}_i - \sqrt{\alpha_i} \hat{\mathbf{x}}_0^{(i)})$
- 8: $\epsilon_i \sim \mathcal{N}(\mathbf{0}, \mathbf{I})$
- 9: $\mathbf{x}_{i-1} \leftarrow \sqrt{\alpha_{i-1}} \hat{\mathbf{x}}_0^{(i)} + \sqrt{1 - \alpha_{i-1}}(\sqrt{1-\zeta} \hat{\mathbf{e}} + \sqrt{\zeta} \epsilon_i)$
- 10: **end for**
- 11: **return** $\hat{\mathbf{x}}_0^{(1)}$

A8.2. DiffPIR [55].

$\sigma_n > 0$ denotes the standard deviation of the measurement noise, and $\omega > 0$ is the data-proximal penalty that trades off data fidelity and the denoiser prior inside the subproblem; $\rho_i \triangleq \omega \sigma_n^2 / \tilde{\sigma}_i^2$ is the iteration-dependent weight used in the proximal objective at step i ; $\hat{\mathbf{x}}_0^{(i)}$ is the score-model denoised prediction of the clean sample at step i (before enforcing data consistency); $\hat{\mathbf{x}}_0^{(i)}$ is the solution of the data-proximal subproblem at step i ; $\hat{\mathbf{e}} = (1 - \alpha_i)^{-1/2}(\mathbf{x}_i - \sqrt{\alpha_i} \hat{\mathbf{x}}_0^{(i)})$ is the effective noise estimate implied by $(\mathbf{x}_i, \hat{\mathbf{x}}_0^{(i)})$; $\epsilon_i \sim \mathcal{N}(\mathbf{0}, \mathbf{I})$ is the fresh Gaussian noise injected at step i ; and $\zeta \in [0, 1]$ mixes deterministic and stochastic updates ($\zeta = 0$ fully deterministic, $\zeta = 1$ fully stochastic). In the GSNR variant, we again use a null-space predictor $\mathbf{G}(\mathbf{y})$ and a weight $\gamma > 0$ to bias the proximal subproblem towards graph-smooth null-space coefficients. In Algorithm 4, we show the GSNR modification of DiffPIR.

In addition to the DPS / DiffPIR variables, GSNR uses: $\mathbf{S} \in \mathbb{R}^{p \times n}$, the graph-smooth null-space projector; $\mathbf{G}^*(\mathbf{y}) \approx \mathbf{S}\mathbf{x}^*$, a learned predictor of the target null coefficient;

Algorithm 5 GSNR–MPGD Sampling null-space and graph regularization

Require: $K, \mathbf{H}, \mathbf{y}, \{\zeta_i\}_{i=1}^K, \{\tilde{\sigma}_i\}_{i=1}^K, \gamma, \gamma_g, \mathbf{S}, \mathbf{G}^*, \mathbf{P}_n, \mathbf{L}$

- 1: $\mathbf{z}_K \sim \mathcal{N}(\mathbf{0}, \mathbf{I})$
- 2: **for** $i = K-1, \dots, 0$ **do**
- 3: $\epsilon_i \sim \mathcal{N}(\mathbf{0}, \mathbf{I})$
- 4: $\mathbf{z}_{0|i} = \frac{1}{\sqrt{\alpha_i}}(\mathbf{z}_i - \sqrt{1 - \alpha_i} \epsilon_\theta(\mathbf{z}_i, i))$
- 5: $\mathbf{z}_{0|i} = \mathbf{z}_{0|i} - \zeta_i \left(\nabla_{\mathbf{z}_{0|i}} \|\mathbf{H}\mathbf{D}(\mathbf{z}_{0|i}) - \mathbf{y}\| + \gamma \|\mathbf{G}^*(\mathbf{y}) - \mathbf{S}\mathbf{D}(\mathbf{z}_{0|i})\|_2^2 + \gamma_g \|\mathbf{P}_n \mathbf{L} \mathbf{D}(\mathbf{z}_{0|i})\|_2^2 \right)$
- 7: $\mathbf{z}_{i-1} = \sqrt{\alpha_{i-1}} \mathbf{z}_{0|i} + \sqrt{1 - \alpha_{i-1} - \sigma_i^2} \epsilon_\theta(\mathbf{z}_i, i) + \sigma_i \epsilon_i$
- 8: **end for**
- 9: **return** $\hat{\mathbf{x}} = \mathbf{D}(\mathbf{z}_0)$



Figure 17. Results using latent-space diffusion models for SR.

icients; $\gamma > 0$, the weight of the null-space matching term; $\gamma_g > 0$, the weight of the null-only graph regularizer; and \mathbf{P}_n and \mathbf{L} , the null projector and graph Laplacian, respectively. The GSNR prior is

$$\gamma \|\mathbf{G}^*(\mathbf{y}) - \mathbf{S}\hat{\mathbf{x}}_0\|_2^2 + \gamma_g \|\mathbf{P}_n \mathbf{L} \hat{\mathbf{x}}_0\|_2^2,$$

for DPS (acting on the current prediction $\hat{\mathbf{x}}_0$), and the analogous expression with \mathbf{x} in the DiffPIR proximal subproblem.

A8.3. MPGD [15].

We evaluate graph-null-space-regularized manifold projected gradient descent (MPGD) [15] for super-resolution. This DM is performed on the latent space [36]. We used the pre-trained latent diffusion model from ² with the CelebA-HQ model. In Algorithm 5, we show the GSNR modification of MPGD. For the experiments, we used the $\mathbf{L} = \mathbf{L}_{\text{Snn}}$ variant with $p = 0.1n$. In Fig. 17, we present the visual outcomes of incorporating GSNR into MPGD. This integration yields up to 0.78 dB SR improvement, indicating that GSNR enhances even competitive end-to-end diffusion-based solvers.

²github.com/CompVis/latent-diffusion

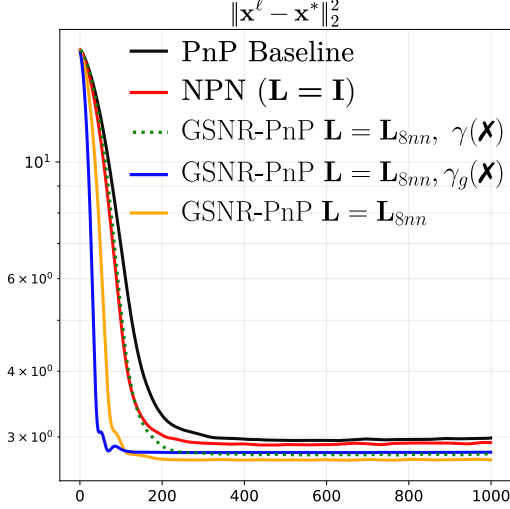


Figure 18. Convergence comparison with PnP, NPN, and GSNR for CS.

Table 3. Experimental settings for GSNR PGD-PnP in demosaicing.

Parameter	Value
γ_g	0.01
γ	0.1
ω	0.01
α	$\frac{1.0}{\ \mathbf{H}\ }$
K (Max iterations)	3000

A9. CS results

Fig. 18 shows an ablation of (8) for the convergence of the reconstruction in PnP-FISTA for CS. PnP Baseline indicates that $\gamma = \gamma_g = 0$. For the GSNR, with only the graph-regularizer (green), $\gamma = 0$ is used. The state-of-the-art, NPN baseline (red) uses the matrix \mathbf{S} from [17] and $\gamma_g = 0$, obtains greater acceleration. GSNR without graph-regularization (blue) uses the proposed operator \mathbf{S} from (6) and the learned network \mathbf{G} with $\gamma_g = 0$. Finally, GSNR with both regularizers, in yellow, utilizes the entire equation (8). From this figure, we can conclude the contribution of each term: if $\frac{\gamma_g}{2} (\mathbf{P}_n \mathbf{x})^\top \mathbf{L} (\mathbf{P}_n \mathbf{x})$ is used, better convergence and reconstruction will be achieved. If $\gamma \|\mathbf{G}(\mathbf{y}) - \mathbf{S}\mathbf{x}\|_2^2$ is used, convergence is further accelerated and reconstruction is improved. Using both terms guarantees good convergence and the best possible reconstruction quality (yellow).

A10. Demosaicing results

In Table 3, the parameter settings are shown for demosaicing experiments. As shown in Table 4, GSNR consistently improves over the baselines. With Lip-DnCNN, GSNR with either \mathbf{L}_{4nn} or \mathbf{L}_{8nn} yields a clear PSNR gain over both

Table 4. Final PSNR (dB) comparison across graph variants and topologies for demosaicing with $n = 64^2$ and $p = 0.5 \cdot 3 \cdot n$.

Method	γ_g	Lip-DnCNN [40]	DRUNet [52]
Baseline	–	39.35	27.91
NPN [17]	✗	39.77	30.12
GSNR w. \mathbf{L}_{4nn}	✗	39.79	30.14
GSNR w. \mathbf{L}_{4nn}	✓	39.89	30.13
GSNR w. \mathbf{L}_{8nn}	✗	39.77	30.27
GSNR w. \mathbf{L}_{8nn}	✓	39.88	30.27

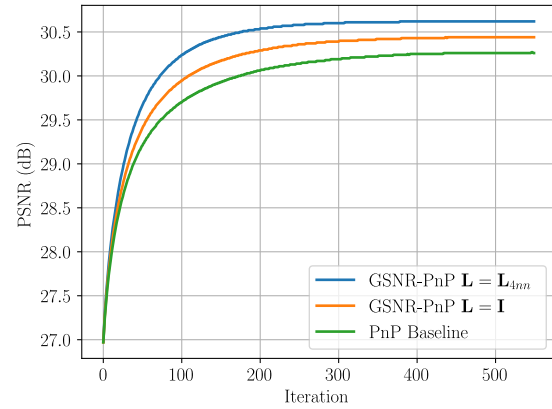
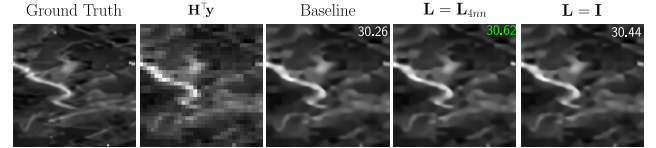


Figure 19. Evaluation of GSNR-PnP on a non-optical imaging example (SAR-like data). Top row: ground-truth image \mathbf{x}^* , back-projection $\mathbf{H}^\top \mathbf{y}$, baseline PnP reconstruction, and GSNR-PnP with \mathbf{L}_{4nn} and $\mathbf{L} = \mathbf{I}$, with PSNR values overlaid. Bottom: PSNR as a function of iteration for GSNR-PnP with \mathbf{L}_{4nn} , GSNR-PnP with $\mathbf{L} = \mathbf{I}$, and the PnP baseline.

PGD-PnP and NPN, showing that graph-limited null-space information brings a systematic boost. With DRUNet, all methods achieve similar absolute PSNR, but GSNR still matches or slightly surpasses NPN across graph topologies. Overall, the improvements are modest yet consistent, underscoring that the main advantage comes from the GSNR null-space representation rather than the specific choice of backbone denoiser or additional graph penalty.

A11. SR results

SAR details for SR: from which we extract 3289 patches of size 128×128 from six satellite scenes for training and 1162 patches from two additional satellite scenes for evaluation.

Figure 19 demonstrates that the proposed graph-smooth null-space representation extends beyond natural images to other imaging domains. The top-row reconstructions show that GSNR-PnP with a grid Laplacian \mathbf{L}_{4nn} produces

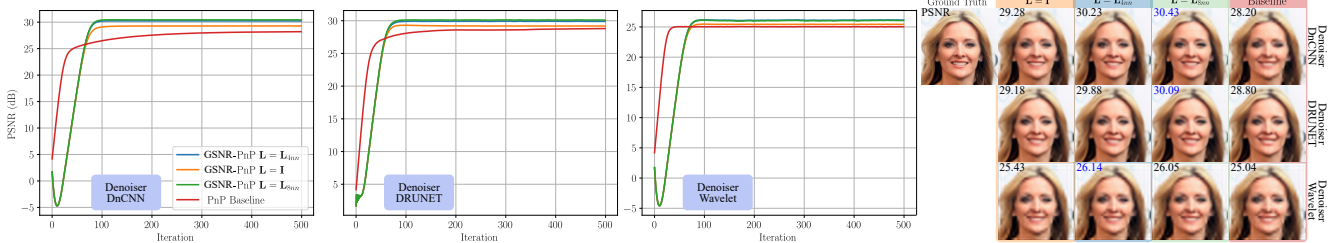


Figure 20. Super-resolution results with GSNR-PnP for different graph Laplacians and denoisers. Left: PSNR versus iteration for GSNR-PnP with $\mathbf{L} = \mathbf{I}$, \mathbf{L}_{4nn} , \mathbf{L}_{8nn} , and the PnP, using (from left to right) DnCNN, DRUNET, and a wavelet denoiser. Right: corresponding reconstructions for a representative face image, with the ground truth at the top-left and PSNR values overlaid on each result.

sharper, less noisy structures than both the baseline PnP solver and the geometry-free $\mathbf{L} = \mathbf{I}$ variant, even though the scene exhibits a speckled texture rather than a smooth photographic content. The corresponding PSNR curves in the bottom panel confirm this behavior quantitatively: GSNR-PnP with \mathbf{L}_{4nn} converges faster and stabilizes at the highest PSNR, while GSNR-PnP with $\mathbf{L} = \mathbf{I}$ still improves over the baseline but remains clearly below the graph-based design. These results indicate that encoding graph-smooth structure in the null-space is beneficial not only for face or natural-image SR, but also for more challenging sensing models such as SAR-like imaging, supporting the broader applicability of GSNR across imaging modalities.

Figure 20 illustrates the effect of the graph-smooth null-space design on super-resolution performance and convergence. The PSNR–iteration plots (left) show that, for all three denoisers, GSNR-PnP with either \mathbf{L}_{4nn} or \mathbf{L}_{8nn} converges to a higher PSNR than both the baseline PnP solver and the geometry-free $\mathbf{L} = \mathbf{I}$ variant. With DnCNN and DRUNET, the graph-based curves not only reach a higher plateau but also exhibit a steeper initial rise, indicating a faster approach to a good solution. Even with the simpler wavelet denoiser, the graph-limited versions match or slightly improve upon the baseline while maintaining stable dynamics. The image grid on the right confirms these trends visually: reconstructions obtained with \mathbf{L}_{4nn} and \mathbf{L}_{8nn} display sharper facial contours and more coherent high-frequency details than both the baseline and $\mathbf{L} = \mathbf{I}$, highlighting the benefit of injecting graph-smooth structure specifically into the null space.

Figure 21 shows the evolution of PSNR for super-resolution on 20 images from the CelebA dataset when DIP is run with and without the proposed graph-smooth null-space representation. The DIP baseline (red) improves rapidly at first but then saturates at a lower PSNR and exhibits noticeable instabilities, including pronounced dips during the late iterations. In contrast, all GSNR-DIP variants converge to a higher PSNR plateau and have much smoother trajectories. Among them, the graph-based choices \mathbf{L}_{4nn} and \mathbf{L}_{8nn} (blue/green) provides the most stable and accurate reconstructions, consistently outperforming both the baseline and the geometry-free $\mathbf{L} = \mathbf{I}$ (orange).

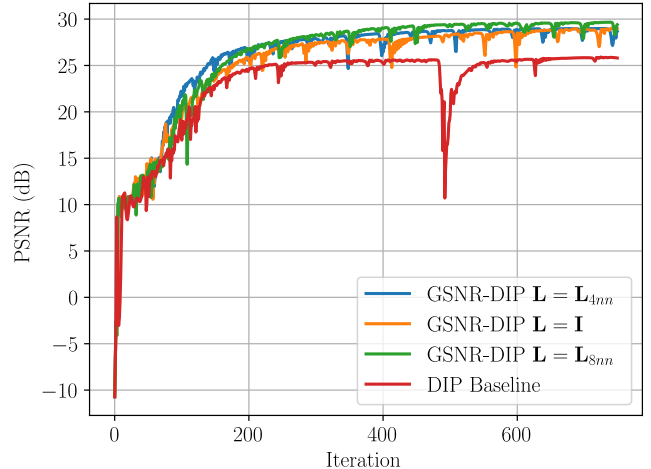


Figure 21. Super-resolution on CelebA (20 images) with Deep Image Prior (DIP). We plot PSNR versus iteration for the standard DIP baseline (red) and the proposed GSNR-DIP variants using different Laplacians: $\mathbf{L} = \mathbf{I}$, \mathbf{L}_{4nn} , and \mathbf{L}_{8nn} .

Table 5. Experimental settings for GSNR PnP-PGD in deblurring.

Parameter	Lip-DnCNN	Wavelet
γ_g	0.1	0.1
γ	0.1	0.1
λ	0.0001	0.001
α	$\frac{1.5}{\ \mathbf{H}\ }$	$\frac{1.5}{\ \mathbf{H}\ }$
K (Max iterations)	800	800

This indicates that enforcing graph-smooth structure specifically in the null space not only improves the final reconstruction quality but also regularizes the DIP optimization itself, mitigating the overfitting and oscillations typically observed in vanilla DIP.

A12. Deblurring results

In the deblurring setting, the sensing matrix \mathbf{H} does not reduce dimensionality, meaning that $n - m = 0$. Consequently, the full set of n eigenvectors of \mathbf{T} was considered when selecting the p smoothest directions.

Experimental settings. Table 5 reports the GSNR PnP-PGD parameters defined to perform image reconstruction.



Figure 22. Deblurring visual results comparing PGD-PnP, GSNR with $\mathbf{L} = \mathbf{I}$ (NPN), and GSNR with $\mathbf{L} = \mathbf{L}_{8nn}$ across two datasets and two denoisers. Best results for each denoiser are highlighted in green. Here, $p = 0.8$.

Table 6. GSNR’s computational cost for SR: offline and online (PnP, one image, 1000 iters).

Metric	/	Resolution	128^2	256^2	512^2
Offline EVD computation (s)			102	1315	22310
Offline RAM (GiB)			0.68	10.88	174.09
PnP runtime (Wavelet) (s)			1.09	1.42	1.96

Visual results. Fig. 22 presents deblurring examples on the CelebA and Places365 datasets for baseline PGD-PnP, GSNR with $\mathbf{L} = \mathbf{I}$ (NPN), and GSNR with $\mathbf{L} = \mathbf{L}_{8nn}$, using either Lip-DnCNN or Wavelet denoisers. The qualitative behavior is consistent across both denoisers. The baseline PGD-PnP produces reconstructions with noticeable residual blur and poor recovery of high-frequency structures, such as eyes and eyebrows in faces or the sharp contours of tree tops in natural scenes.

Using GSNR with $\mathbf{L} = \mathbf{I}$ improves the reconstruction of high-frequency components, producing visually sharper results. However, because the identity Laplacian imposes no geometric constraints, the recovered details are not necessarily aligned with the true image structures. This often leads to overly sharp but inaccurate features that do not reflect the desired image geometry. In contrast, GSNR with graph-based Laplacians, such as \mathbf{L}_{8nn} , enforces geometric consistency through graph-smoothness. As a result, the restored high-frequency structures are both sharp and coherent with the true image content, yielding the most faithful reconstructions among the tested methods. This advantage is reflected not only visually but also quantitatively, with GSNR achieving the highest PSNR values. A noteworthy observation is that GSNR enables reconstructions using a simple Wavelet denoiser to surpass the performance of reconstructions obtained with a more advanced neural-network denoiser like DnCNN. This highlights GSNR’s capacity to adapt to and significantly strengthen any reconstruction method, offering robust improvements across a broad range of inverse problem solvers.

Table 7. Final PSNR on DIV2K for deblurring (G trained on Places365).

	Lip-DnCNN	Wavelet
Baseline (PnP-PGD)	31.23	30.39
NPN [17]	33.05	32.90
GSNR (\mathbf{L}_{8nn})	33.69	33.65

A13. Scalability and computational cost

We use 128^2 images to enable controlled comparisons. GSNR introduces only a low *online* overhead at inference time, since the subspace computation is performed *offline* once per $(\mathbf{H}, \mathbf{L}, n, p)$ and reused. We only compute the p smoothest eigenvectors (selected by the coverage plateau in Algorithm 1), so memory scales as $\mathcal{O}(pn)$. We never materialize \mathbf{P}_n or \mathbf{T} : we wrap $\mathbf{T}\mathbf{x} = \mathbf{P}_n\mathbf{L}\mathbf{P}_n\mathbf{x}$ as an implicit LinearOperator and compute the first p eigenpairs via ARPACK `eigsh` (A5), exploiting sparse \mathbf{L} for fast matrix operations. Table 6 reports scaling to 512^2 ; the online cost remains low, whereas the offline EVD increases with resolution. For $n^2 \geq 1024^2$, EVD computation becomes costly with ARPACK. Future work will focus on efficient approximate EVD computation.

A14. Dataset generalization and neural network ablation

To assess whether GSNR regularization transfers across image distributions, we performed a cross-dataset experiment for deblurring setting. We trained the neural network G on Places365 and then evaluated GSNR on DIV2K [1]. The results in Table 7 show that the gains provided by GSNR remain consistent under this distribution shift, indicating that the learned null-space predictor generalizes to diverse natural images.

We further examine the robustness of GSNR with respect to the choice of neural network architecture for G. In Figure 23, we replace the default U-Net with three recent architectures: DFPIR [47], EVSSM [22], and AdaIR [10]. As expected, stronger predictors yield more accurate null-

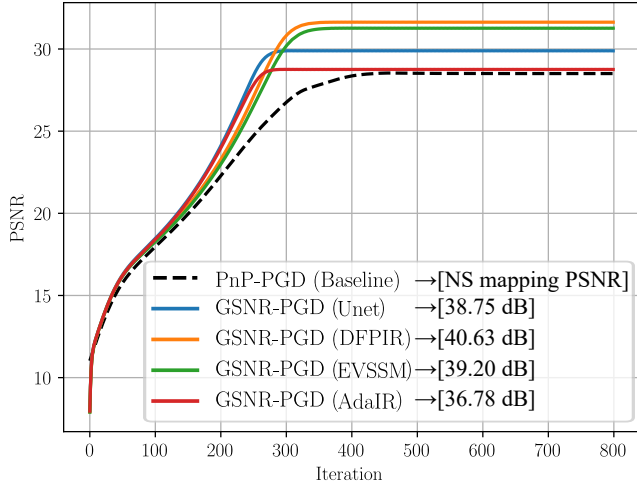


Figure 23. PSNR with G ablation in Places for the deblurring task.

space estimates, as reflected by the higher PSNR values for the null-space mapping (see Fig. 23 legend). Importantly, GSNR improves PnP reconstruction quality and accelerates convergence for all tested backbones, suggesting its benefits arise from the proposed GSNR regularization rather than a specific architecture.

A15. Inexact forward operator

In many inverse problems, the forward operator available to the reconstruction algorithm is only an approximation of the true sensing physics. In practice, the nominal sensing matrix \mathbf{H} can deviate from the actual measurement operator due to calibration errors, hardware tolerances, or other unmodeled effects. Such mismatches are particularly detrimental because they propagate into the algorithmic components derived from \mathbf{H} , including null-space projectors and any structure imposed through them, and can therefore undermine both accuracy and convergence. To quantify this effect in a concrete setting, Fig. 24 evaluates deblurring under operator mismatch. Measurements are generated as $\mathbf{y} = (\mathbf{H} + \mathbf{H}_\xi)\mathbf{x}^* + \omega$, with $\mathbf{H}_\xi \sim \mathcal{N}(0, 0.005^2)$ while recovery still assumes the nominal \mathbf{H} . This mismatch yields imperfect estimates of \mathbf{P}_n and \mathbf{S} , which in turn degrades the null-space representation used by GSNR. Despite these compounded imperfections, GSNR remains effective, improving performance by approximately 1 dB and converging in fewer iterations.

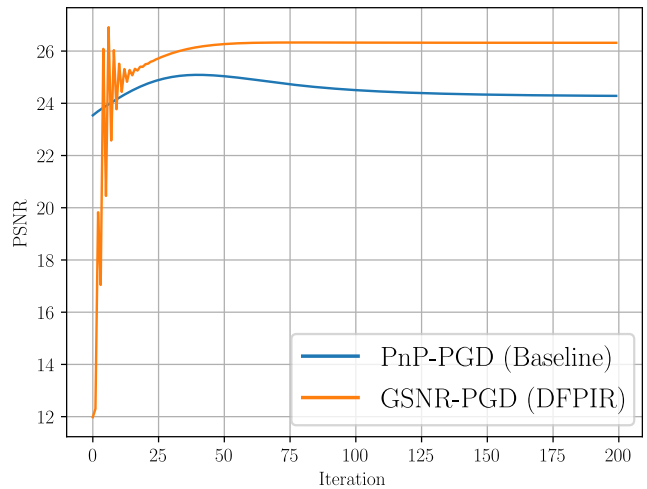


Figure 24. PSNR in deblurring with inexact forward operator.